Journal Pre-proof

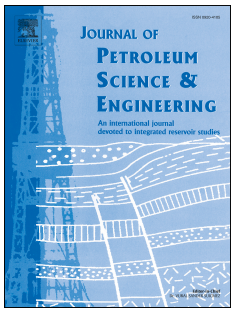

The differential diagenesis controls on the physical properties of lithofacies in sandstone reservoirs from the Jurassic Shaximiao Formation, western Sichuan depression, China

Xiaoju Zhang, Meiyan Fu, Hucheng Deng, Zhongdong Li, Shuang Zhao, Jon G. Gluyas, Tairan Ye

PII: S0920-4105(20)30485-X

DOI: https://doi.org/10.1016/j.petrol.2020.107413

Reference: PETROL 107413

To appear in: *Journal of Petroleum Science and Engineering*

Received Date: 25 August 2019

Revised Date: 25 March 2020

Accepted Date: 12 May 2020

Please cite this article as: Zhang, X., Fu, M., Deng, H., Li, Z., Zhao, S., Gluyas, J.G., Ye, T., The differential diagenesis controls on the physical properties of lithofacies in sandstone reservoirs from the Jurassic Shaximiao Formation, western Sichuan depression, China, *Journal of Petroleum Science and Engineering* (2020), doi: https://doi.org/10.1016/j.petrol.2020.107413.

Credit author statement

Xiaoju Zhang: Writing-original draft; Writing-review & editing; Data curation, Methodology, and Investigation.

Meiyan Fu: Conceptualization, Methodology, Writing-Reviewing and Editing, and Investigation, and Supervision.

Hucheng Deng: Conceptualization and Supervision.

Zhongdong Li: Methodology and Supervision.

Shuang Zhao: Resources, Data curation, and Investigation.

Jon G. Gluyas: Writing-Reviewing and Editing.

Tairan Ye: Resources and Data curation.

The differential diagenesis controls on the physical properties of lithofacies in sandstone reservoirs from the Jurassic Shaximiao Formation, Western Sichuan Depression, China

Xiaoju Zhang[a,b], Meiyan Fu[a,b*], Hucheng Deng[a,b], Zhongdong Li[a,b], Shuang Zhao[c], Jon G. Gluyas[d], Tairan Ye[c]

[a.] *State Key Laboratory of Oil and Gas Reservoir Geology and Exploitation (Chengdu University of Technology), Chengdu 610059, PR China;*

[b.] *College of Energy, Chengdu University of Technology, Chengdu 610059, PR China;*

[c.] *Research Institute of Exploration and Development, Southwest Branch Company of Sinopec, Chengdu 610041, PR China;*

[d.] *Earth Science Department, Durham University, DH1 3LE, UK.*

[*]*Corresponding author (e-mail: fumeiyan08@cdut.cn).*

Abstract

The Jurassic Shaximiao Formation on the eastern slope of western Sichuan depression in western Sichuan Basin of China develops a single or overlapping channel sandstones with strong internal heterogeneity. This study aims to reveal the origin of the differences of physical properties within the sandstone reservoirs under different assemblies of lithofacies. Based on analysis of sedimentary structure and grain size, the lithofacies are classified into nine types. Based on the classification of lithofacies formed under different energy of sedimentary environment and mechanical differentiation, the effect of early compaction on physical properties of sandstone reservoirs is confirmed. It is suggested that the physical

properties of lithofacies can be influenced by differential diagenesis in different lithofacies assemblies. The rate of early compaction depends on the grain sorting and compositional maturity. The massive bedded lithofacies are prone to be of good grain sorting and high compositional maturity with relatively low compaction rate of 70.91% to 72.75%. There are relatively high porosities and permeabilities of sandstones in the lithofacies assembly containing massive bedded lithofacies. Because of the export of diagenetic fluid along the bedding plane of parallel bedded sandstones, there would be relatively intensive dissolution of sandstones developed with parallel bedded lithofacies. Even if the development of parallel bedded sandstones could enhance the dissolution, yet they are subjected to relatively strong compaction, leading to the low proportion of intergranular pores. The permeability of sandstones within the lithofacies assembly containing parallel bedded lithofacies seems to be low. The porosity and permeability of sandstones within the lithofacies assembly containing horizontal bedded lithofacies are both poorer than other assemblies, caused by strong compaction, cementation and weak dissolution. The direction of bedding, argillaceous contents, and the capacity of resistance to compaction are the key factors controlling the physical property of high-quality sandstone reservoirs. The research conclusions can be used to interpret the genesis of different physical properties of sandstone reservoirs in other similar gas fields.

Keywords: Western Sichuan depression; Shaximiao Formation; Lithofacies assembly; Compaction; Differential diagenesis; Physical properties

1. Introduction

Many natural gas reservoirs in China are sandstone reservoirs with strong internal heterogeneity (Zhang et al., 2018; Wang et al., 2019). A great difference in physical properties can be found in a same set of sandstones (Bu, 2018; Wang et al., 2019). It is widely recognized that the physical properties of sandstone reservoirs are generally correlative with lithofacies types (Gould et al., 2012; Stroker et al., 2013; Burki and Darwish, 2017).

Many research efforts have been invested in the past to study the lithofacies within sandstones (Yoshida, 2000; Miall, 2006; Turner and Tester, 2006; Okoro and Igwe, 2014). The studies regarding the effect of lithofacies on the porosity and permeability have been made great progress. Liu et al. (2016) proposed a new characterization method of permeability controlled by lithofacies. Several studies revealed that the reservoirs developing massive bedded medium-coarse grained sandstones have good physical properties even after deeply burial diagenesis (Taylor et al., 2010; Gao and Lin, 2012). However, the reservoirs developing parallel bedded medium-fine grained sandstones are prone to be of relatively poor physical properties (Taylor et al., 2010; Gao and Lin, 2012). Moreover, it is clarified that the porosity of massive bedded fine-silt grained sandstones is lower than that of cross bedded siltstones (Yin et al., 2016).

The role of sedimentary structure within single lithofacies on physical property has been discussed in the last two decades. Several studies revealed that grain sizes, grain sorting, and matrix contents of lithofacies are related to energy of sedimentary environment (Kathleen et al., 2010; Taylor et al., 2010; Zhang et al., 2014). The compaction of sandstones can be affected by grain sorting (Saïaga1 et al., 2016). A small amount of primary pores can be preserved after relatively weak compaction during burial diagenesis (Umar et al., 2011;

Henares et al., 2014; Henares et al., 2016). Dixon et al. (1989) and Ozkan et al. (2011) revealed that there are different compaction and primary porosity in different lithofacies. The weak compaction of massive bedded medium-coarse grained sandstones is related to good grain sorting and high compositional maturity (Taylor et al., 2010; Saïaga1 et al., 2016), and some primary pores can be preserved. On the other hand, the compaction has a greatly impact on the flow of diagenetic fluid, which can influence the late burial diagenesis (Shanley, et al., 2004; Marcussen et al., 2010). The rock fragments and feldspar are prone to dissolve because of their reaction with diagenetic fluid during the late burial diagenesis (Higgs et al., 2007; Li et al., 2019). Moreover, the strength of cementation and the clay content would also be the important factors for porosity reduction (Nabawy and Barakat, 2017). However, the physical property of sandstones with same sedimentary structure and grain size in the different lithofacies assemblies has not been well understood, and the change of flow rate of diagenetic fluid, compaction of sandstones in adjacent lithofacies would modify the diagenesis.

This paper focuses on the differential diagenesis of original lithofacies within different lithofacies assembly from the Jurassic Shaximiao Formation in Zhongjiang and Gaomiaozi gas fields on the eastern slope of western Sichuan depression, China. In these gas fields, the high-yield areas are relatively scarce, and the production rates and the reserves of individual wells in the same set of sandbodies significantly vary. Each lithofacies has a particular gas production in these sandstone reservoirs (Bu, 2018; Liu et al., 2018). In this study, the grain sizes and grain sorting are used to reflect the sedimentary features of lithofacies. During burial diagenesis, the compaction rate and dissolution rate could be calculated to quantify the diagenetic change of sandstones within different lithofacies. The main factors control the

sedimentary structure were discussed, including the energy of sedimentary environment, the distance of transportation and the erosion of sediments. The differential diagenesis of lithofacies assemblies was investigated to reveal the modification of original lithofacies during diagenesis.

2. Geological setting

Figure 1 shows that the location of the eastern slope of western Sichuan depression and the stratigraphic column of the Jurassic Shaximiao Formation (Liu et al., 2018). As can be seen in Figure 1a, the western Sichuan depression is located in the western part of Sichuan Basin of China, and surrounded by the east of the Longmen Mountain Thrust Belt and the west of the middle Sichuan uplift in Sichuan Basin (Guo et al., 2018; Liu et al., 2018). The western Sichuan depression underwent multi-stage tectonic movements from the Mesozoic. These tectonic movements include the Indosinian orogeny, the Yanshanian orogeny, and the Himalayan orogeny (Ratschbacher et al., 2003). The western Sichuan depression contains six tectonic zones. These tectonic zones include three inversion tectonic zones, two subsidence zones, and one slope zone as shown in Figure 1b. The study area is mainly located in the eastern slope zone. The tectonic subzones developed in the study area include Fenggu tectonic subzone, Hexingchang-Gaomiaozi tectonic subzone, Zhixinchang-Shiquanchang tectonic subzone, and Zhongjiang-Huilong tectonic subzone as shown in Figure 1c. There are two gas fields located in the Gaomiaozi and the Zhongjiang area, with gas generation from the Jurassic Shaximiao Formation. There are multifarious morphologies of channels (i.e., straight channels and sinuous channels) with dispersing sandbodies developing in these gas fields

(Figure 1c).

The sequence stratigraphy of the Jurassic Shaximiao Formation in the study area is shown in Figure 1d. The sandstones of the Jurassic Shaximiao Formation on the eastern slope were deposited within the channel and bay mud between channels of a delta (Liu et al., 2018). The Upper Shaximiao Formation is composed of the rhythm layer alternated by sandstone and mudstone (Figure 1d). Tabular and trough cross bedding, parallel bedding, scouring structures, and lenticular conglomerate on the scouring surface of the sandstones can be observed in the Upper Shaximiao Formation (Lü et al., 2015). The Lower Shaximiao Formation consists of 2-4 sets of superimposed gray to grayish-purple, thick-bedded, fine-medium grained subarkose, arkose, purple siltstone, and mudstone (Liu et al., 2018). Cross bedding are usually observed in the Lower Shaximiao Formation (Du et al., 2013; Liu et al., 2018). The sandstones of the Upper and the Lower Shaximiao Formation both develop the normal-graded bedding sequence (Lü et al., 2015; Liu et al., 2018).

Moreover, the burial history of the Jurassic sequences was characterized by an initial period of moderate to rapid subsidence from the Early Jurassic to Late Jurassic, and the maximum burial depth of Jurassic strata is approximately 2600m (Lü et al., 2015). Then there was a period of slow subsidence from Late Jurassic to Eocene. The subsidence phase was followed by uplift and erosion of 1000–2000m of the sedimentary strata from Eocene to Neogene (Shen et al., 2011. Lü et al., 2015).

3. Samples and methods

This study was carried out based on the data collected from 28 wells in the Gaomiaozi

and Zhongjiang areas as shown in Figure 1c. In this study, the testing information of samples (i.e., porosity and permeability, mercury injection, and thin sections) was shown in Tables 1a, 1b, 1c, 1d, and 1e.

In this work, the characteristics of the cores from 28 drilling wells were described. The total length of these cores was roughly 509 m. There are two lithologies in these 28 cored wells, i.e., sandstones and mudstones. Four types of sedimentary bedding can be observed, i.e., massive bedding, tabular cross bedding, parallel bedding, and horizontal bedding. Schwarzacher (1953) suggested that the stratification of sedimentary bedding can be divided into three types based on their thickness, i.e., small-scale stratification (with a thickness smaller than 3 cm), medium-scale stratification (with a thickness of 3 cm to 10 cm), and large-scale stratification (with a thickness lager than 10 cm). On the basis of this criterion, the tabular cross bedding in the study area can be defined as large tabular cross bedding and small tabular cross bedding.

The thin section identification of 65 samples from 10 cored wells shows that the main lithologies include medium-grained and fine-grained sandstones. Based on the data of 80 thin sections from those 10 wells (including the previous 65 samples), there are three types of components in sandstones observed in this study area. They are quartz with a roughly content of 51%, feldspar with a roughly content of 27%, and rock fragments with a roughly content of 22%. There are five types of rock fragments, including metamorphic rock fragments, effusive rock fragments, flint rock fragments, mudstone rock fragments, and siltstone rock fragments. Furthermore, there is a relatively low content of cements in sandstones of the study area ranging from 1% to 5%. The cements are mainly composed of calcite and siliceous. The thin

section identification was performed using the Axio Scope A1 pol polarizing microscope (Carl Zeiss, Germany).

The grain sorting of sandstones can be quantitatively described by the grain sorting coefficient, which could be calculated by Equation (1) (Visher, 1969; Scherer, 1987). In Equation (1), P_{25} and P_{75} refer to the particle diameter within the cumulative probabilities of 25% and 75%, respectively, which can be obtained from the cumulative percentage curves of grain size of sandstones. The cumulative percentage curves of grain size of sandstones within different lithofacies were obtained by analyzing the particle sizes of 65 thin sections from 10 cored wells.

$$S_0 = P_{25}/P_{75} \tag{1}$$

where S_0 is grain sorting coefficient; and P_{25} and P_{75} are particle diameter with the cumulative probabilities of 25% and 75%, respectively.

The compositional maturity of sandstones could be quantitatively characterized by the content of each component (i.e., quartz, feldspar, and rock fragments) in sandstones as shown in Equation (2) (Taylor et al., 2010). In Equation (2), Q, F, and R refer to quartz, feldspar, and rock fragments, respectively. The contents of these components were counted point-by-point based on 80 thin sections from 10 cored wells.

$$C_m = Q/(F + R) \tag{2}$$

where C_m is compositional maturity; Q is quartz; F is feldspar; and R is rock fragments.

The primary porosity is controlled by the grain sorting, and that of different lithofacies can be calculated by the grain sorting coefficient as given by Equation (3) (Beard and Weyl, 1973; Scherer, 1987).

$$\emptyset_0 = 20.91 + 22.90/S_0 \quad (R^2=0.965) \tag{3}$$

where $\emptyset_0$ is primary porosity.

The strength of compaction can be quantified by the compaction rate as shown in Equations (4) and (5) (Beard and Weyl, 1973; Houseknecht, 1987; Houseknecht, 1988). As shown in Equations (4) and (5), the intergranular volume after the compaction during burial diagenesis (V_{inter}) is equal to the sum of the volume of intergranular pores (V_i), the volume of cements (V_c), and the volume of matrix (V_m). These parameters were obtained using an image analysis system based on 80 thin sections from 10 cored wells.

$$C_{rate} = \frac{(\emptyset_0 - V_{inter})}{\emptyset_0} \times 100\% \tag{4}$$

$$V_{inter} = V_i + V_c + V_m \tag{5}$$

where C_{rate} is compaction rate; V_{inter} is the intergranular volume after the compaction during burial diagenesis; V_i is the volume of intergranular pores; V_c is the volume of cements; and V_m is the volume of matrix.

The strength of dissolution can be quantified by the dissolution rate as shown in Equation (6) (Houseknecht, 1987; Ehrenberg, 1989). As shown in Equation (6), the porosity of dissolved pores (D_{pore}) was calculated based on 80 thin sections from 10 cored wells. The primary pores and dissolved pores can be distinguished under polarizing microscope. Residual dissolved minerals could be found in the intergranular dissolved pores, and there is various irregular pore morphologies in intragranular dissolved pores. However, the primary pores with regular pore morphology have no residual dissolved minerals.

$$D_{rate} = D_{pore}/\emptyset_0 \tag{6}$$

where D_{rate} is dissolution rate; and D_{pore} is the porosity of dissolved pores.

The porosity and permeability of samples were measured by gas flow method (Ling et al., 2013; Li et al., 2019). The porosity was measured using the ULTRAPORE-300 helium-porosity automatic measuring instrument (Core Lab, USA), while the permeability was measured using the DP-DYX-6G gas permeability measuring instrument (i.e., gas permeameter) (Beijing Yaou Depeng Technology Company, China). The porosity of samples from 26 cored wells was measured, while the permeability of samples from 23 cored wells was measured.

The mercury injection experiments were conducted on 88 sandstone samples from 13 cored wells to determine their pore-throat radius. Capillary injection curves of 8 samples were drawn based on the data obtained by mercury injection experiments. The mercury injection experiments were conducted using the ASPE730 automated system for pore examination (Coretest, USA). The maximum value of the mercury pressure is 220MPa.

4. Results

4.1. Types of lithofacies and lithofacies assembly

An individual lithofacies is considered to be a rock unit defined on the basis of its distinctive lithological features, including mineral composition, grain size, bedding characteristics, and sedimentary structures (Vaziri, 2011; Menkem, et al., 2013). In this study, the types of lithofacies are identified based on the bedding structure (Figure 2) and grain size. In the study area, there are nine types of lithofacies including: (1) large tabular cross bedded medium-grained sandstone (S_{ltm}), (2) small tabular cross bedded medium-grained sandstone (S_{stm}), (3) large tabular cross bedded fine-grained sandstone (S_{ltf}), (4) small tabular cross

bedded fine-grained sandstone (S_{stf}), (5) massive bedded medium-grained sandstone (S_{mm}), (6) massive bedded fine-grained sandstone (S_{mf}), (7) parallel bedded medium-grained sandstone (S_{pm}), (8) parallel bedded fine-grained sandstone (S_{pf}), and (9) horizontal bedded fine-grained sandstone (S_{hf}).

There is more than one lithofacies developed in an individual sandbody vertically. Based on the statistics of the vertically co-developed lithofacies in an individual sandbody, there are ten types of lithofacies assembly developing in the study area, including S_{mm} + S_{pm} (Type #1), S_{mm} + S_{mf} (Type #2), S_{ltm} + S_{mm} (Type #3), S_{stm} + S_{mm} (Type #4), S_{stm} + S_{pm} (Type #5), S_{stm} + S_{pf} (Type #6), S_{mm} + S_{pf} (Type #7), S_{ltm} + S_{stf} (Type #8), S_{ltf} + S_{stf} (Type #9), and S_{pf} + S_{hf} + S_{mf} (Type #10). Based on the similar sedimentary bedding assemblies of each lithofacies assemblies, these lithofacies assemblies were further concluded into four types of coexisting lithofacies, including (a) massive bedded lithofacies + parallel bedded lithofacies, (b) massive bedded lithofacies + tabular cross bedded lithofacies, (c) tabular cross bedded lithofacies + parallel bedded lithofacies, and (d) massive bedded lithofacies +horizontal bedded lithofacies +parallel bedded lithofacies.

4.2. Compaction rate and dissolution rate of different lithofacies

The compaction rates and dissolution rates of different lithofacies are shown in Table 2. There are low compaction rate (with a range of 72.13% to 72.28%) and high dissolution rate (with a range of 8.36% to 16.63%) in massive bedded medium-fine grained sandstones. The large/small tabular cross bedded medium-fine grained sandstones have relatively high compaction rate (ranging from 74.58% to 83.01%) and relatively low dissolution rate (ranging from 8.50% to 11.30%). The parallel bedded medium-fine grained sandstones and horizontal

bedded fine-grained sandstones have high compaction rate (ranging from 82.67% to 88.31%) and low dissolution rate (ranging from 5.75% to 5.84%).

4.3. Pore structure of different lithofacies

The pore structures (i.e., pore diameter and pore-throat radius) of massive bedded lithofacies and large/small tabular cross bedded lithofacies are better than those of parallel bedded lithofacies and horizontal bedded lithofacies (Figures 3, 4, and 5).

Figure 3 indicates that capillary injection curves of different lithofacies in terms of the cross-plot of the applied mercury pressure versus the incremental mercury saturation. As shown in Figure 3, the capillary pressure curves of different lithofacies are significantly different. The results show that the pore sorting of massive bedded sandstones and large/small tabular cross bedded sandstones with larger pore radius is better than that of parallel bedded sandstones and horizontal bedded sandstones (Figure 3). On the other hand, the pore radius of medium-grained lithofacies with better pore sorting is larger than that of fine-grained lithofacies (Figure 3).

Figure 4a shows the pore diameters of different lithofacies, and Figures 4b, 4c, and 4d show the cross-plot of median pore-throat radii and pore sorting coefficients of different lithofacies. As shown in Figure 4a, there is a large pore diameter (roughly 177.2 μm) of massive bedded medium-fine grained sandstones. The pore diameter of large tabular cross bedded medium-fine grained sandstones is roughly 140μm. However, the small tabular cross bedded medium-fine grained sandstones and parallel bedded medium-fine grained sandstones have relatively small pore diameters, whose the pore diameters are roughly 72.6 μm and 68.3 μm, respectively. It can be seen from Figures 4b, 4c, and 4d that the median pore-throat radius

of medium-grained lithofacies is larger than that of fine-grained lithofacies. In general, the median pore-throat radii of massive bedded medium-fine grained sandstones and large/small tabular cross bedded medium-fine grained sandstones are relatively larger than those of parallel bedded medium-fine grained sandstones and horizontal bedded fine-grained sandstones (Figures 4b, 4c, and 4d). As can be seen in (Figures 4b, 4c, and 4d), the median pore-throat radii of massive bedded medium-fine grained sandstones, large tabular cross bedded medium-fine grained sandstones, and small tabular cross bedded medium-fine grained sandstones are roughly 0.077 μm, 0.154 μm, and 0.111 μm, respectively. However, the median pore-throat radii of parallel bedded medium-fine grained sandstones and horizontal bedded fine-grained sandstones are roughly 0.069 μm and 0.035 μm, respectively.

4.4. Physical properties of different lithofacies

Physical properties of massive bedded lithofacies and large/small tabular cross bedded lithofacies are better than those of parallel bedded lithofacies and horizontal bedded lithofacies (Figures 6 and 7).

Figure 6 shows the statistics on physical properties of nine types of lithofacies. The average porosity of S_{mm}, S_{ltm}, and S_{stm} is 10.4%, 11.1%, and 8.4%, respectively (Figure 6a). The average permeability of these three types of lithofacies is 1.21 mD, 1.13 mD, and 0.73 mD (Figure 6b), respectively. Physical properties of these three types of lithofacies are best within all the lithofacies. S_{pm}, S_{pf}, S_{mf}, S_{stf}, and S_{ltf} have good physical properties, with average porosity of 9.3%, 8.1%, 8.4%, 7.5%, and 6.8%, respectively (Figure 6a), and average permeability of 0.34 mD, 0.18 mD, 0.43 mD, 0.22 mD, and 0.17 mD, respectively (Figure 6b). S_{hf} has an average porosity of 5.9% (Figure 6a) and an average permeability of 0.1 mD

(Figure 6b).

Figures 7a and 7b show the statistics on physical properties of different lithofacies types within medium-grained sandstones and fine-grained sandstones, respectively. As shown in Figures 7a and 7b, the porosity and permeability of lithofacies within medium-grained sandstones rank from largest to smallest as follows: S_{mm}, S_{ltm}, S_{stm}, and S_{pm} (Figure 7a); while for fine-grained sandstones, the order of porosity and permeability from largest to smallest is S_{mf}, S_{ltf}, S_{stf}, S_{pf}, and S_{hf} (Figure 7b). Figures 7c, 7d, 7e, and 7f indicate that the porosity and permeability of medium-grained lithofacies are better than those of fine-grained lithofacies.

5. Discussions

5.1. Energy of sedimentary environment and mechanical differentiation controls the formation of different lithofacies

The relationship among energy of sedimentary environment, bedform, and sedimentary bedding is shown in Figure 8. The recursive sequence of bedform can be present as follows with an increasing current velocity when the grain size and the depth of sediments are constant: lower plane bed or no movement, sand ripple, sand dune with sand ripple, sand dune, upper plane bed, and antidune (Gilbert, 1914; Simons et al., 1965; Allen, 1968). Horizontal bedding, small tabular cross bedding, and large tabular cross bedding occur in transquil flow condition (i.e., Froude number (Fr) <1) (Simons et al., 1965). Horizontal bedding can form when the bottom of bed is smooth and no sediments laterally move with weakest energy of sedimentary environment. The horizontal bedding frequently occurs in argillaceous sediments (Okoro and Igwe, 2014). The small tabular cross bedding can form resulting from the

movement of sand ripples with the parallel crest line under relatively strong energy of sedimentary environment. The large tabular cross bedding can form resulting from the movement of sand dune with sand ripples and sand dune with the parallel crest line under strong energy of sedimentary environment (Bell, 1991). No undulation can be present in the bottom of bed when the current velocity reaches the certain limit in rapid flow condition (i.e., Froude number (Fr) >1) (Simons et al., 1965; Belderson and Johnson, 1982). The upper plane bed can remain in stratigraphic records called parallel bedding under very strong energy of sedimentary environment (Simons et al., 1965).

Based on statistics of different lithofacies developed in channels with different sinuosity index in the study area, in general, tabular cross bedded lithofacies and massive bedded lithofacies developed in sinuous channels; while parallel bedded lithofacies and horizontal bedded lithofacies developed in straight channels. The slope of straight channels is larger than that of sinuous channels, and the vertical stratification of flow in straight channels is greater than that in sinuous channels, resulting in the high deposition rates in straight channels (Figure 9) (Kneller, 2003; Timár, 2003; Strauba et al., 2011). The relatively weak mechanical differentiation of sediments in straight channels will lead to the weak erosion caused by short distance of sediment transportation and deposition relatively close to the provenance of sedimentation (Strauba et al., 2011). Therefore, the sediments in straight channels would be prone to be of relatively poor grain sorting. The lateral accretion is prone to occur in sinuous channels (Timár, 2003; Strauba et al., 2011). The strong mechanical differentiation of sediments in sinuous channels could induce a strong erosion related to the relatively complex and long distance of sediment transportation (Strauba et al., 2011), resulting in good grain

sorting of sediments.

The characteristics of bedding and sedimentary structures caused by mechanical transportation are difficult to record in massive bedded sandstones as the entire unit is massive in nature (Srivastava and Mankar, 2015). The massive bedded sandstone represents a product of grain flows and high-density turbidity flows (Maill, 2000; Okoro and Igwe, 2014). The interpretation of Bouma sequences (Slatt et al., 1997) genesis has been heavily reported, and the findings also revealed that massive bedding could form caused by the deposits of high-density turbidity current (Middleton, 1967; Mutti and Lucchi, 1978; Lowe, 1982). The massive bedded sandstone is characterized by the rapid accumulation of sediments and it is a product of gravity current, resulting from the vertical aggradation of sediments (Vaziri, 2011; Menkem et al., 2013).

It is commonly believed that the grain size can reflect the energy of sedimentary environment (Slattery and Burt, 1997; Phillips and Walling, 1999; Zhang et al., 2014). The movement of sediments is mainly affected by the traction and gravity. The depositional velocity of particles in stagnant water is shown in Equation (7) (Slattery and Burt, 1997). Figure 10 shows the relationship between energy of sedimentary environment and grain size. As shown in Equation (7) and Figure 10a, the depositional velocity of medium-grained particles is larger than that of fine-grained particles. The particles can be transported when the current velocity is large enough and the traction is larger than the gravity as shown in Figure 10a. Equation (8) shows the relationship among Froude number, water depth, and current velocity. The Froude number increases with an increasing current velocity when the water depth is constant. As shown in Figure 10b, a positive correlation could be found between

current velocity and grain size (Hjulstrom, 1939; Sundbory, 1956). As a consequence, there is a positive correlation between Froude number and grain size. The strength of energy of sedimentary environment could be quantitatively reflected by the Froude number. The larger the Froude number is, the stronger the energy of sedimentary environment is.

$$u = \frac{1}{18}(\rho_s - \rho_f) \times g \times d^2 / \eta \quad (7)$$

$$Fr = v/\sqrt{h \cdot g} \quad (8)$$

where u is depositional velocity of particles; ρ_s is the density of particles; ρ_f is the density of current; η is the viscosity of current; g is gravity acceleration; d is the diameter of particles; Fr is Froude number; v is current velocity; h is water depth; and g is gravity acceleration.

As discussed above, under the strong energy of sedimentary environment, the grain size of particles is prone to be coarse. As shown in Figures 10c and 10d, under the strong energy of sedimentary environment, the grain size of the large tabular cross bedded sandstone from the well J14 is coarse-grained, with the median grain diameter of roughly 0.65 mm. In contrast, as can be seen in Figures 10e and 10f, under the weak energy of sedimentary environment, the grain size of the horizontal bedded sandstone from the well G2 is fine-grained, with the median grain diameter of roughly 0.245 mm.

5.2. The effect of grain sorting on early compaction

The relationship among the grain sorting coefficient, compaction rate, and median grain size of different lithofacies is shown in Figure 11. Based on the calculation and analysis, the grain sorting coefficient of sandstones has a correlation with compaction rate as shown in Figure 11a, implying that the grain sorting can influence the compaction of sandstones during

burial diagenesis. The compaction becomes stronger with gradually poorer grain sorting. The grain sorting of medium-grained lithofacies is better than that of fine-grained lithofacies as shown in Figure 11b, while the compaction of fine-grained lithofacies is stronger than that of medium-grained lithofacies (Table 2). Through the observation of thin sections, the particles are more closely arranged in fine-grained lithofacies (Figures 5a, 5b, 5c, and 5d; Figures 5e, 5f, 5g, and 5h). In contrast, the particles are loosely arranged in massive bedded medium-fine grained sandstones (Figures 5a and 5e), and numerous primary pores are preserved (Table 2).

There is a relationship between grain sorting of sandstones and the median grain size of particles as shown in Figure 11b. The particles with different grain sizes can be transported by the traction in terms of different transportation ways (i.e., scrolling, leaping, and suspension) under the same energy of sedimentary environment (Moss et al., 1979; Asadi et al., 2011). The coarse clastic materials (i.e., gravel and coarse-grained particle) are transported by the traction in terms of scrolling; the medium-fine grained particles are transported by the traction in terms of leaping; and such silt particles are transported by the traction in terms of suspension (Everts, 1973). Among them, sandstones transported by leaping have good grain sorting under relatively strong energy of sedimentary environment, whilst sandstones transported by suspension have poor grain sorting under weak energy of sedimentary environment (Everts, 1973). Therefore, the differences of grain sorting could be caused by different transportation ways of particles (Everts, 1973; Allen, 1982).

On the other hand, long transportation distance and strong erosion of sediments during the process of transportation would lead to strong mechanical differentiation, resulting in good grain sorting of sediments (Kathleen et al., 2010). As the product of mechanical

differentiation during this process, the grain sorting of different lithofacies will be distinctive. The grain sorting of massive bedded sandstones and tabular cross bedded sandstones is better than that of parallel bedded sandstones and horizontal bedded sandstones, resulting from the strength of mechanical differentiation, as discussed in section 5.1.

As a result, the compaction of different lithofacies could depend on the grain sorting during the burial process (Table 2 and Figure 11a). The compaction rate of massive bedded medium-fine grained sandstones is relatively low, with the best grain sorting among all lithofacies (Table 2 and Figure 11b). The tabular cross bedded medium-fine grained sandstones have the moderate compaction rate with the moderate grain sorting (Table 2 and Figure 11b). The grain sorting of parallel bedded medium-fine grained sandstones and horizontal bedded fine-grained sandstones are poorest within all lithofacies (Figure 11b). Figures 5d and 5h show that particles are closely arranged in these two types of lithofacies with a strong compaction (Table 2).

Except for the grain sorting, particles can also be arranged with the orientation and stratiform in parallel bedded sandstones and horizontal bedded sandstones because of sedimentary differentiation (Asadi et al., 2011). However, particles of tabular cross bedded sandstones and massive bedded sandstones can be arranged with no orientation and stratiform.

5.3. The effect of compositional maturity of particles and early compaction on dissolution

The pore evolution of different lithofacies would be different, resulting from the dissolution, cementation, and compaction during the burial diagenesis. Among those diagenetic changes, the dissolution, which has a positive contribution to the secondary

425 porosity, is a most important factor influencing the physical properties of sandstones.
426 Furthermore, there is no correlation between the volume of cements and the volume of pores
427 as shown in Table 2, thus, the effect of cements on the porosity reduction has been out of
428 consideration in this study.

429 The compositional maturity of particles is equal to the content of quartz divided by the
430 sum of the content of unstable components (i.e., feldspar and rock fragments) as shown in
431 Equation (2). The compositional maturity of sandstones could be influenced by weathering
432 and erosion of sediments during the process of transportation and sedimentation (Carroll and
433 Bohacs, 1999; Ketzer et al., 2003; Liu et al., 2005; Kathleen et al., 2010). The original
434 compositional maturity of different lithofacies were calculated after the unstable components
435 affected by the weathering before the beginning of transport. The unstable components could
436 decompose by the weathering during the transportation of sediments (Taylor et al., 2000;
437 Salem et al., 2005; Mansurbeg et al., 2006). As a result, in the massive bedded medium-fine
438 grained sandstones and large/small tabular cross bedded medium-fine grained sandstones,
439 most of the unstable components (i.e., feldspar + rock fragments) would decompose resulting
440 from the strong weathering and intensive erosion of sediments.

441 The dissolution rate is equal to the dissolved porosity divided by the primary porosity as
442 shown in Equation (6). In this study, the data used to conduct the correlation analysis among
443 compositional maturity of particles, early compaction, and dissolution were on the basis of the
444 average values of each parameters of nine types of lithofacies as shown in Table 2.

445 As can be seen from Figure 12, the results show that the dissolution rate has a positive
446 relationship with the compositional maturity of sandstones (Figure 12a), and a negative

447 relationship with the compaction rate (Figure 12b). The compaction has a greatly impact on
448 the flow of diagenetic fluid (Shanley, et al., 2004; Marcussen et al., 2010), leading to the
449 different degree of dissolution. However, the compositional maturity of sandstones could
450 influence the compaction, resulting from the different content of plastic particles related to the
451 compositional maturity. The compositional maturity of lithofacies in the study area is
452 distinctive, as shown in Figure 13.

453 As a result, there is a relatively high compositional maturity of massive bedded
454 medium-fine grained sandstones with weak early compaction and strong dissolution (Table 2).
455 The compositional maturity of large/small tabular cross bedded medium-fine grained
456 sandstones, which has relatively weak early compaction and dissolution (Table 2), is lower
457 than that of massive bedded medium-fine grained sandstone (Figure 13). The compositional
458 maturity of parallel bedded medium-fine grained sandstones and horizontal bedded
459 fine-grained sandstones is the lowest among all the lithofacies as shown in Figure 13, while
460 these two lithofacies have relatively weak dissolution and strong early compaction (Table 2).
461

462 *5.4. The differential diagenesis of original lithofacies within different lithofacies assemblies*

463 Although the compaction and dissolution of single lithofacies was controlled by grain
464 sorting and compositional maturity, there were different diagenesis features of lithofacies
465 assemblies. The compaction of massive bedded and tabular cross bedded medium-fine grained
466 sandstones is lowest within all lithofacies, as a result, the porosities and permeabilities of
467 sandstones developed with massive bedded and tabular cross bedded medium-fine grained
468 sandstones are highest among whole lithofacies assemblies (Figures 14a, 14b, 14c, 14d, and
469 14e). There are large coefficient of skewness and median pore-throat radius of sandstones

within the lithofacies assembly with massive bedded lithofacies as shown in Figures 14f.

Dissolution of sandstones with same sedimentary structure in different lithofacies assemblies significantly vary. As shown in Figure 15a, the dissolution rates of massive bedded sandstone are distinct in the case of massive bedded sandstones developed with different lithofacies. It seems that the development of parallel bedded lithofacies is beneficial for the dissolution rate of sandstones (Figure 15a), implying that the direction of bedding might have influenced the dissolution. The migration of diagenetic fluid along the bedding plane could result in the export of dissolved material, leading to there was a great number of new dissolved pores generated (c.f. Shanley, et al., 2004; Marcussen et al., 2010; Yuan et al., 2015). In contrast, the retention of dissolved material could precipitate again as by-products, e.g. quartz and clay minerals. After the relatively strong dissolution, the compositional maturities of the tabular cross bedded medium-grained sandstones developed with parallel bedded sandstones are higher than that developed with massive sandstones (Figure 15b). As the evidence from the thin sections, Figures 5i and 5j show the different dissolution rate in the tabular cross bedded medium-grained sandstones developed with massive bedded sandstones and parallel bedded sandstones. Although the total numbers of pores in these two samples are similar, the dissolved pores dominated in the assembly of tabular cross bedded medium-grained sandstones and parallel bedded sandstones, while few intergranular pores developed in this assembly resulting from the slightly stronger compaction. Therefore, the development of parallel bedded sandstones could promote compaction, even though the dissolution was enhanced. It indicates that the dissolved materials have been carried off with the compaction. As a result, the porosities of tabular cross bedded medium-grained sandstones

in the two different lithofacies assembly are almost similar, the permeabilities of tabular cross bedded medium-grained sandstones developed with parallel bedded sandstones are lower than that developed with massive bedded sandstones, caused by the dominated dissolved pores with poor pore connectivity. Meanwhile, there are low coefficient of skewness and median pore-throat radius of sandstones within the lithofacies assembly of tabular cross bedded medium-grained sandstones and parallel bedded sandstones, resulting from the mean size of dissolved pores is relatively small comparing with intragranular pores (Figures 14f).

The compaction of horizontal bedded fine-grained sandstones was strongest within whole lithofacies. As a consequence, the lithofacies adjacent to horizontal bedded fine-grained sandstones are subjected to relatively strong compaction (Figure 15c). The parallel bedded fine-grained sandstones developed with horizontal bedded fine-grained sandstones have lower porosities and permeabilities than that developed with massive bedded sandstones and tabular cross bedded sandstones (Figure 14e). The strong compaction without relatively intensive dissolution occurs in the parallel bedded fine-grained sandstones developed with horizontal bedded fine-grained sandstones. Due to the thin-bedded argillaceous occurred in the horizontal bedded fine-grained sandstones, the calcium and silicon released by clay mineral diagenesis will result in the precipitation of calcite and quartz in the void spaces of adjacent sandstones (c.f. Mohamand and Peter, 1997; Samakinde et al., 2016; Jiu et al., 2018). It is suggested that the strong compaction of horizontal bedded fine-grained sandstones would result in the diagenetic fluid containing sufficient calcium and silicon charge into the adjacent parallel bedded fine-grained sandstones, and then the cementation was enhanced. As show in Figure 5l, these cements were observed in the parallel bedded fine-grained sandstones.

514 The differential diagenesis of lithofacies assemblies have an important influence on the
515 pore number and physical properties of sandstones. Due to the relatively weak compaction,
516 the assembly of massive bedded and tabular cross bedded lithofacies has the best physical
517 properties, with porosity of 8.01-12.37% and permeability of 0.25-1.98 mD (Figure 16). The
518 assemblies of massive bedded and parallel bedded lithofacies, tabular cross bedded and
519 parallel bedded lithofacies have moderate physical properties, with porosity of 6.57-12.62%
520 and permeability of 0.02-0.29 mD (Figure 16), resulting from the relatively strong
521 compaction and relatively strong dissolution. There are strong compaction, cementation and
522 weak dissolution of sandstones within the lithofacies assembly containing horizontal bedded
523 lithofacies, leading to the poorest physical properties (porosity of 3.30-9.98%, permeability of
524 0.05-0.17 mD) (Figures 16).

525 There are also some studies have revealed the difference of physical properties in
526 sandstone reservoirs based on sedimentary facies and diagenetic facies in individual fields or
527 layers (Kalefa et al., 2006; Zou et al., 2008; Kalefa et al., 2009; Gao and Lin, 2012; Lai et al.,
528 2016). However, less research efforts have invested to regard the lithofacies assembly as a
529 diagenetic system. In this study, through the analysis of sedimentation and diagenesis of the
530 lithofacies assemblies, the differential diagenesis controls on the physical properties of
531 lithofacies in sandstone reservoirs was revealed to conclude as a schematic diagram in Figure
532 16. The results could interpret the differences of the physical properties of sandstone
533 reservoirs in other similar gas fields.

534

535 **6. Conclusions**

(1) There are nine types of lithofacies in the Jurassic Shaximiao Formation. The physical properties and pore structures of these types of lithofacies rank from good to poor as follows: massive bedded lithofacies, tabular cross bedded lithofacies, parallel bedded lithofacies, and horizontal bedded lithofacies. The formation of lithofacies with different physical properties is controlled by the energy of sedimentary environment and mechanical differentiation, resulting in different grain sorting and compositional maturity of lithofacies. Under good grain sorting and high compositional maturity, the early compaction becomes relatively weak, resulting in a lot of primary pores preserved.

(2) The differential diagenesis of lithofacies assemblies controls on the physical properties of lithofacies. Strong capacity of resistance to compaction leads to the high porosity and permeability of sandstones developed with massive bedded lithofacies. The direction of bedding could influence the degree of dissolution. The flow of diagenetic fluid along the bedding plane of parallel bedded lithofacies resulted in relatively intensive dissolution, with high proportion of dissolved pores of sandstones and low permeability. However, resulting from the strong compaction, cementation and weak dissolution, the sandstones developed with horizontal bedded lithofacies containing thin-bedded argillaceous have lowest porosity and permeability.

Acknowledgements

This study was supported by the project from Southwest Branch Company of Sinopec (China) (Grant No. 34450000-15-ZC0607-0005) and the project of unconventional oil and gas geological research from Scientific Research Innovation Team of Provincial Governed

Colleges, Education Department of Sichuan Province (China) (Grant No. 14TD0008). The authors sincerely appreciate Sujuan Ye, Huaji Li, and Tingkuan Cao from Southwest Branch Company of Sinopec for their help when the research was carried out. Special thanks should go to Ruixue Li who has put considerable time and effort into revising English language of the manuscript.

References

Allen, J. R. L., 1968. Current ripples: their relation to patterns of water and sediment motion. Amsterdam, North-Holland.

Allen, J. R. L., 1982. Sedimentary structures, pp.75–135. Elsevier, Amsterdam.

Ainsworth, R. B., Vakarelov, B.K., Nanason, R. A., 2011. Dynamic spatial and temporal prediction of changes in depositional processes on clastic shorelines: Toward improved subsurface uncertainty reduction and management. AAPG Bulletin, 95(2), 267–297.

Asadi, H., Moussavi, A., Ghadiri, H., Rose, C.W., 2011. Flow-driven soil erosion processes and the size selectivity of sediment. Journal of Hydrology, 406(1), 73–81.

Beard, D. C., Weyl, P. K., 1973. Influence of texture on porosity and permeability of unconsolidated sand. AAPG Bulletin, 57(2), 349–369.

Belderson, R. H., Johnson, M. A., 1982. Bedforms, In Offshore Tidal Sands:Process and Deposits, New York, Chapman and Hall, 27–57.

Bell, C. M., 1991. The relationship between sedimentary structure, transport direction and dune types in Mesozoic aeolian sandstones, Atacama Region, Chile. Sedimentary, 38, 289–300.

Burki, M., Darwish, M., 2017. Electrofacies vs. lithofacies sandstone reservoir characterization companion sequence, Arshad gas/oil field, Central Sirt Basin, Libya. Journal of African Earth Science, 130, 319–336.

Bu, T., 2018. Sand body configuration of delta channel of Jurassic Shaximiao Group in east slope of West Sichuan Depression. Fault-Block Oil & Gas Field, 25(5), 564–567 (in Chinese with English abstract).

Carroll, A. R., Bohacs, K. M., 1999. Stratigraphic classification of ancient lakes: Balancing tectonic and climatic controls. Geology, 27, 99−102.

Dixon, S. A., Summers, D. M., Surdam, R. C., 1989. Diagenesis and preservation of porosity in Norphlet Formation (Upper Jurassic), southern Alabama. AAPG Bulletin, 73(6), 707−728.

Everts, C. H., 1973. Particle overpassing on flat granular boundaries. Am. Soc. Civ. Engrs., 99, 425–438.

Ehrenberg, S. N., 1989. Assessing the relative importance of compaction processes and cementation to reduction of porosity in sandstones: discussion; compaction and porosity evolution of pliocene sandstones，Ventura Basin，California: Discussion. AAPG Bulletin, 73(10), 1274–127.

Folk, R.L., Ward, W. C., 1957. Brazos River bar, a study in the significance of grain size parameters. J. Sed. Petro., 27, 3–27.

Gilbert, G. K., 1914. The transportation of rock fragments by running water. USGS Professional Paper, 1–

595 86.
596 Gould, K. M., Piper, D. J. W., Pe-Piper, G., 2012. Lateral variation in sandstone lithofacies from
597 conventional core, Scotian Basin: implications for reservoir quality and connectivity. Canadian Journal
598 of Earth Sciences. 49(12), 1478–1503.
599 Gao, L., Lin, C., 2012. A Facies Analysis and Sedimentary Architecture of the Paleogene Dainan
600 Formation in the Gaoyou Depression, North Jiangsu Basin, Eastern China. Petroleum Science and
601 Technology, 30(14), 1486–1497.
602 Guo, Y.C., Song, L.C., Fang, X.X., et al., 2018. Conventionally trapped natural gas accumulations in the
603 Jurassic tight sandstone reservoirs: a case study from the center of the Western Sichuan Basin, SW China.
604 Energy Exploration & Exploitation, 36(5), 1022–1039.
605 Hjulstrom, F., 1939. Transportation of rock fragments by moving water, In Recent Marine Sediments. A
606 Symposium Spec. Pub.Econ. Paleont. Miner, Tulsa, 5–31.
607 Harms, J.C., Fahnestoek, R.K., 1965. Stratification, bedforms, and flow phenomena (with an example from
608 the Rio Grande) , SEPM, Special Publication 12, 1977, p. 84–115.
609 Houseknecht, D.W., 1987. Assessing the relative importance of compaction processes and cementation to
610 reduction of porosity in sandstones. AAPG Bulletin, 71(6), 501–510.
611 Houseknecht, D. W., 1988. Intergranular pressure solution in four quartzose sandstones. Journal of
612 Sedimentary Research, 58(2), 228–246.
613 Higgs, K. E., Zwingmann, H., Reyes, A. G., et al, 2007. Diagenesis, porosity evolution, and petroleum
614 emplacement in tight gas reservoirs, Taranaki Basin, New Zealand. Journal of Sedimentary Research,
615 77(12), 1003–1025.
616 Henares, S., Caracciolo, L., Cultrone, G., et al., 2014. The role of diagenesis and depositional facies on
617 pore system evolution in a Triassic outcrop analogue (SE Spain). Marine & Petroleum Geology, 51(2),
618 136–151.
619 Henares, S., Caracciolo, L., Viseras, C., et al., 2016. Diagenetic constraints on heterogeneous reservoir
620 quality assessment: a Triassic outcrop analogue of meandering fluvial reservoir. AAPG Bulletin, 100(9),
621 1377–1398.
622 Jiu, B., Huang, W. H., Shi, J., et al., 2018. Growth mechanism of siliceous cement in tight sandstone and its
623 influence on reservoir physical properties. Energies, 11, 3133.
624 Krumbein, W. C., 1934. Size frequency distributions of sediments. Journal of Sedimentary Research, 4(2),
625 65–77.
626 Ketzer, J. M., Morad, S., Amorosi, A., et al., 2003. Predictive diagenetic claymineral distribution in
627 siliciclastic rocks within a sequence stratigraphic framework. Intermational Associational of
628 Sedimentologists, 15(3-4), 43–61.
629 Kneller, B., 2003. The influence of flow parameters on turbidite slope channel architecture. Marine and
630 Petroleum Geology, 20, 901–910.
631 Kalefa, M. A., Ghali, E., Howri, M., et al., 2006. Distribution of diagenetic alterations in glaciogenic
632 sandstones within a depositional facies and sequence stratigraphic framework: Evidence from the upper
633 ordovician of the Murzuq Basin, SW Libya. Sedimentary Geology, 190, 323–351.
634 Kalefa, M. A., Ghali, E., Sadoon, M., et al., 2009. Distribution of diagenetic alteration within depositional
635 facies and sequence stratigraphic framework of fluvial sandstones: Evidence from the petrohan
636 terrigenous group, lower Triassic, NW Bulgaria. Marine and Petroleum Geology, 26, 1212–1227.
637 Kathleen, G.， Georgia, P., David, J. W. P., 2010. Relationship of diagenetic chlorite rims to depositional
638 facies in Lower Cretaceous reservoir sandstones of the Scotian basin. Sedimentology, 57, 587–610.

Lowe, D. R., 1982. Sediment gravity flows: II. Depositional models with special reference to the deposits of high-density turbidity current. Journal of Sedimentary Research, 52(1), 279–297.

Liu, Z. F., Colin, C., Trentesaux, A., et al., 2005. Late Quaternary climatic control on erosion and weathering in the eastern Tibetan Plateau and the Mekong Basin. Quaternary Research, 63(3), Pages 316–328.

Ling, K. G., He, J., Pei, P., 2013. Determining the permeability of tight rock with gas transient flow. Journal of Natural Gas Science and Engineering, 15, 1–7.

Lü, Z. X., Ye, S. J., Yang, X., et al., 2015. Quantification and timing of porosity evolution in tight sand gas reservoirs: an example from the Middle Jurassic Shaximiao Formation, western Sichuan, China. Petroleum Science, 12(2), 207–217.

Liu, Y. C., Luo, X. b., Kang, K., et al., 2016. A new method of permeability characterization in sandstone reservoir based on petrographic constraints. Petroleum Geology and Recovery Efficiency, 23(5), 93–97 (in Chinese with English abstract).

Lai, J., Wang, G. W., Chai, Y., et al., 2016. Prediction of diagenetic facies using well logs: Evidences from Upper Triassic Yanchang Formation Chang 8 Sandstones in Jiyuan Region, Ordos Basin, China. Oil & Gas Science and Technology, 71(3), 34–51.

Liu, J.L., Yin, W., Ji, Y.L., et al., 2018. Sequence architecture and sedimentary characteristics of a Middle Jurassic incised valley, western Sichuan depression, China. Petroleum Science, 15, 230–251.

Li, Y., Chang, X. C., Yin, W., et al., 2019. Quantitative identification of diagenetic facies and controls on reservoir quality for tight sandstones: A case study of the Triassic Chang 9 oil layer, Zhenjing area, Ordos Basin. Marine and Petroleum Geology, 102, 680–694.

McCammon, R. B., 1962. Efficiencies of percentile measures for describing the mean size and sorting of sedimentary particles. Journal of Geology, 70, 453–465.

Middleton, G. V., 1967. Experiments on density and turbidity currents III: deposition of sediment. Canadian Journal of Earth Science, 4, 475–505.

Mutti, E., Lucchi, R. F., 1978. Turbidities of the northern Apennines: introduction to facies analysis. International Geology Review, 20, 125–166.

Moss, A. J., Walker, P. H., Hutka, J., 1979. Raindrop-stimulated transportation in shallow water flows: an experimental study. Sedimentary Geology, 22(3), 165–184.

Middleton, B., 1980. Murray, Origin of Sedimentary Rocks. New Jersey: PRENT ICE HALL, INC., Englewood Cliffs, 71.

Mohamand, R. R., Peter, T., 1997. Origin of quartz cement in the Terrawarra sandstone, southern Cooper Basin, South Australia. Jouranal of Sediment Research, 67(1), 168–177.

Maill, A.D., 2000. Principles of sedimentary Basin Analysis, 3rd ed., Springer–Verlag Berlin Heidelberg, pp. 616p.

Miall, A. D., 2006. Reconstructing the architecture and sequence stratigraphy of the preserved fluvial record as a tool for reservoir development: a reality check. AAPG Bulletin, 90(7), 989–1002.

Mansurbeg, H., Elghali, M. A. K., Morad, S., et al., 2006. The impact of meteoric water on the diagenetic alteration in deep water, marine siliciclastic turbidites. Journal of Geochemical Exploration. 89(1-3), 254–258.

Marcussen, Ø., Maast, T. E., Mondol, N. H., et al., 2010. Changes in physical properties of a reservoir sandstone as a function of burial depth–The Etive Formation, northern North Sea. Marine and Petroleum Geology, 27(8), 1725–1735.

Menkem, E.F., Sebag, D., Ngatcha, B.N., et al., 2013. Lithofacies and depositional environment of

683 volcano-sedmentary deposits of Se Mayo Oulo Basin. American Journal of Geosciences, 3(2), 23–29.
684 Nabawy, B.S., Barakat, M.Kh, 2017. Formation Evaluation using conventional and special core analyses:
685 Belayim Formation as a case study, Gulf of Suez, Egypt. Arabian Journal of Geosciences 10 (25), 1–23.
686 Ozkan, A., Cumella, S. P., Milliken, K. L., et al., 2011. Prediction of lithofacies and reservoir quality using
687 well logs, Late Cretaceous Williams Fork Formation, Mamm Creek field, Piceance Basin, Colorado.
688 AAPG Bulletin, 95(10), 1699–1723.
689 Okoro, A. U., Igwe, E. O. 2014. Lithofacies and depositional environment of the Amasiri Sandstone,
690 southern Benue Trough, Nigeria. Journal of African Earth Sciences, 100, 179–190.
691 Phillips, J. M., Walling, D. E., 1999. The particle size characteristics of fine-grained channel deposits in the
692 River Exe Basin, Devon, UK. Hydrological Processes, 13(1), 1–19.
693 Ratschbacher, L., Hacker, B. R., Calvert, A., et al., 2003. Tectonics of the Qinling (Central China):
694 Tectonostratigraphy, geochronology and deformation history. Tectonophysics, 366, 1–53.
695 Schwarzacher, W., 1953. Cross-Bedding and Grain Size in the Lower Cretaceous Sands of East Anglia.
696 Geological Magazine, 90(5), 322–330.
697 Simons, D. B., Richardson, E. V., Nordin JR, C. F., 1965. Sedimentary structures generated by flow in
698 alluvial channels. Special Publications, 12, 34–52.
699 Southard, J.B., 1971. Representation of bed configuration in depth velocity-size diagram. Journal of
700 Sedimentary Research, 41(4), 903–915.
701 Scherer, M., 1987. Parameters influencing porosity in sandstone a model for sandstone porosity prediction.
702 AAPG Bulletin, 71(5), 485–491.
703 Slattery, M. C., Burt, T. P., 1997. Particle size characteristics of suspended sediment in hillslope runoff and
704 stream flow. Earth Surface Processes and Landforms, 22(8), 705–719.
705 Slatt, R. M., Weimer, P., Stone, C. G., 1997. Reinterpretation of depositional processes in a classic flysch
706 sequence (Pennsylvanian Jackfork Group), Ouachita Mountains, Arkansas and Oklahoma: discussion 1.
707 AAPG Bulletin, 81(3), 449–459.
708 Sun, D. H., Bloemendal, J., Rea, D. K., et al., 2002. Grain-size distribution function of polymodal
709 sediments in hydraulic and Aeolian environment, and numerical partitioning of the sedimentary
710 components. Sedimentary Geology, 152(3/4), 163–277.
711 Shanley, K. W., Cluff, R. M., Robinson, J. W., 2004. Factors controlling prolific gas production from low
712 permeability sandstone reservoirs: Implications for resource assessment, prospect development, and risk
713 analysis. AAPG Bulletin, 88(8), 1083–1121.
714 Salem, A. M., Ketzer, J. M., Morad, S., et al., 2005. Diagenesis and reservoir-quality evolution of
715 incised-valley sandstones: evidence from the abu madi gas reservoirs (upper miocene), the nile delta
716 basin，Egypt. Journal of Sedimentary Research. 75(7), 572–584.
717 Shen, Z.M., Liu, Y., Liu, S.B., et al., 2011. Denudation recovery of Himalayan periods in middle section of
718 western Sichuan depression. Comput Tech Geophys Geochem Explor, 33(2),189 (in Chinese with
719 English abstract).
720 Strauba, K. M., Mohrigb, D., Buttlesb, J., et al., 2011. Quantifying the influence of channel sinuosity on the
721 depositional mechanics of channelized turbidity currents: A laboratory study. Marine and Petroleum
722 Geology 28, 744–760.
723 Stroker, T. M., Harris, N. B., Elliott, W.C., et al., 2013. Diagenesis of a tight gas sand reservoir: Upper
724 Cretaceous Mesaverde Group, Piceance Basin, Colorado. Marine & Petroleum Geology, 40(1), 48–68.
725 Srivastava, A. K., Mankar, R. S., 2015. Lithofacies architecture and depositional environment of Late
726 Cretaceous Lameta Formation, central India. Arabian Journal of Geosciences, 8(1), 207–226.

Saïagal, J., Brigauda, B., Éric Portier, et al., 2016. Sedimentological control on the diagenesis and reservoir quality of tidal sandstones of the Upper Cape Hay Formation (Permian, Bonaparte Basin, Australia). Marine & Petroleum Geology, 77, 597–624.

Samakinde, C., Opuwari, M., Van Bever Donker, J. M., 2016. The effects of clay diagenesis on petrophysical properties of the lower Cretaceous sandstone reservoirs, Orange Basin, South Africa. South African Journal of Geology, 119 (1), 187–202.

Taylor, K. G., Gawthorpe, R. L., Curtis, C. D., et al., 2000. Carbonate cementation in a sequence stratigraphic framework: upper cretaceous sandstones, book cliffs, Utah-Colorado. Journal of Sedimentary Research, 70(2), 360–372.

Timár, G., 2003. Controls on channel sinuosity changes: a case study of the Tisza River, the Great Hungarian Plain. Quaternary Science Reviews, 22(20), 2199–2207.

Turner, B. R., Tester, G. N., 2006. The table rocks sandstone: A fluvial, friction-dominated lobate mouth bar sandbody in the Westphalian B Coal Measures, NE England. Sedimentary Geology, 190(1-4), 97–119.

Taylor, T. R., Giles, M. R., Hathon, L. A., et al., 2010. Sandstone diagenesis and reservoir quality prediction: Models, myths, and reality. AAPG Bulletin, 94(8), 1093–1132.

Umar, M., Friis, H., Khan, A. S., et al., 2011. The effects of diagenesis on the reservoir characters in sandstones of the late cretaceous Pab formation, Kirthar fold belt, southern Pakistan. Journal of Asian Earth Sciences, 40, 622–635.

Visher, G. S., 1969. Grain-size distribution and depositional processes, Journal of Sedimentary petrology, 39(3), 1074–1106.

Vaziri, S.H., 2011. Sedimentary structures and depositional environment of the Ashin Formation in Nakhlak area, Central Iranian Journal of Earth Sciences, 3, 1–9.

Williams, G., 1967. Flume experiments on the transport of a coarse sand. USUGS Prof. Paper 652-B, 1–31.

Wang, X. Z., Qiao, X. Y., Mi, N. Z., et al., 2019. Technologies for the benefit development of low-permeability tight sandstone gas reservoirs in the Yan'an Gas Field, Ordos Basin. Natural Gas Industry, B6, 272–281.

Yoshida, S., 2000. Sequence and facies architecture of the upper Blackhawk formation and lower Castlegate sandstone (upper Cretaceous), Book Cliffs, Utah, USA. Sedimentary Geology, 136, 239–276.

Yuan, G. H., Cao, Y. C., Gluyas, J., et al., 2015. Feldspar dissolution, authigenic clays, and quartz cemnets in open and closed sandstone geochemical systems during diagenesis: Typical examples from two sags in Bohai Bay Basin, East China. AAPG Bulletin, 99(11), 2121–2154.

Yin, S. L., Chen, G. Y., Zhang, L., et al., 2016. The controlling effect of lithofacies architecture on high quality tight sandstone reservoirs: A case study of second member of the Upper Triassic of Xujiahe Formation, western Sichuan Depression, China. Natural Gas Geoscience, 27(7), 1179–1189 (in Chinese with English abstract).

Zou, C. N., Tao, S. Z., Zhou, H., et al, 2008. Genesis, classification, and evaluation method of diagenetic facies. Petroleum Exploration and Development, 35(5), 526–540.

Zhang, X., Lin, C. M., Dalrymple, R. W., et al., 2014. Facies architecture and depositional model of a macrotidal incised-valley succession (Qiantang River estuary, eastern China), and differences from other macrotidal systems. GSA Bulletin, 126 (3-4), 499–522.

Zhang, Y. C., Zeng, J. H., Dai, Z. X., et al., 2018. Experimental investigation on oil migration and accumulation in tight sandstones. Journal of Petroleum Science and Engineering, 160, 267–275.

FIGURES CAPTIONS

Figure 1 The location of the eastern slope of western Sichuan depression and the stratigraphic column of the Jurassic Shaximiao Formation (Liu et al., 2018): (a) The location of the western Sichuan depression in Sichuan Basin; (b) The map shows that six tectonic zones of the western Sichuan depression and tectonic subzones developed in the study area; (c) The locations of 28 cored wells; and (d) The stratigraphic column of the Jurassic Shaximiao Formation in the study area. The Upper Shaximiao Formation is divided into Js_1 and Js_2, and the Lower Shaximiao Formation is named by Js_3.There are straight channels and sinuous channels with the dispersing sandbodies developing in the study area as shown in Figure1c, and the channels shown in this figure developed in Js_1^4 sand group and Js_3^{3-2} sand group of the study area.

Figure 2 Photos of sandstones with different sedimentary bedding: (a) Well J12, depth: 2665.55-2665.85m, massive bedding; (b) Well G14, depth: 2818.24-2818.56m, tabular cross bedding; (c) Well G11, depth: 2773.22-2773.62m, parallel bedding; and (d) Well G2, depth: 2582.68-2582.83, horizontal bedding.

Figure 3 The Cross-plot of the applied mercury pressure versus the incremental mercury saturation indicating capillary injection curves of different lithofacies: (a) Capillary injection curves of massive bedded sandstones; (b) Capillary injection curves of large tabular cross bedded sandstones; (c) Capillary injection curves of small tabular cross bedded sandstones; and (d) Capillary injection curves of parallel bedded sandstones and horizontal bedded sandstones. P-applied mercury pressure; S-incremental mercury saturation; N-total number of samples. The data of capillary injection curves of different lithofacies obtained from 8

samples of 7 cored wells in total.

Figure 4 Statistics on the pore diameter of different lithofacies types and r50-Sp cross-plots of the different grain size of sandstones with the same bedding: (a) Statistics on the pore diameter of different lithofacies; (b)-(d) r50-Sp cross-plots of different grain size of sandstones with the same bedding, (b) Large/small tabular cross bedded sandstones, (c) Massive bedded sandstones, and (d) Parallel bedded sandstones and horizontal bedded sandstones. r50-median pore-throat radius. Sp-pore sorting coefficient. The red circle refers to the medium-grained lithofacies, and the yellow circle refers to the fine-grained lithofacies. N-total number of samples. The data of pore diameter of different lithofacies (i.e., max, min, and average values of pore diameter of each lithofacies) obtained from 42 samples in Figure 4a.

Figure 5 Thin section photos show pore structure of different lithofacies types: (a) Well J14, depth: 2606.585m, massive bedded medium-grained sandstone, total number of pores-708; (b) Well J11, 2656.77m, large tabular cross bedded medium-grained sandstone, total number of pores-783; (c) Well J14, 2595.745m, small tabular cross bedded medium-grained sandstone, total number of pores-532; (d) Well G11, 2768.17m, parallel bedded medium-grained sandstone, total number of pores-231; (e) Well J14, 2608.935m, massive bedded fine-grained sandstone, total number of pores-362; (f) Well G9, 2848.35-2848.38m, large tabular cross bedded fine-grained sandstone, total number of pores-95; (g) Well J11, 2649.64m, small tabular cross bedded fine-grained sandstone, total number of pores-306; and (h) Well G1, 3170.9 -3170.93m, parallel bedded fine-grained sandstone, no pores. (i) Well J11, 2654.16mm, tabular cross bedded medium-grained sandstone in the lithofacies assembly with massive

bedded lithofacies, total number of pores-609, the pore type is composed of intergranular pores, good pore connectivity can be seen in this figure; (j) Well J11, 2654.99 mm, tabular cross bedded medium-grained sandstone in the lithofacies assembly with parallel bedded lithofacies, total number of pores-604, the pore type is composed of intergranular dissolved pores, poor pore connectivity can be seen in this figure; (k) Well J14, 2608.065 mm, parallel bedded fine-grained sandstone in the assembly of massive bedded lithofacies + parallel bedded lithofacies, total number of pores-294, the pore type is composed of intergranular dissolved pores and intergranular dissolved pores, poor pore connectivity can be seen in this figure; (l) Well J14, 2608.485 mm, parallel bedded fine-grained sandstone in the assembly of massive bedded lithofacies + parallel bedded lithofacies +horizontal bedded lithofacies, a few of pores and poor pore connectivity can be seen in this figure. Red arrow refers to the intergranular pores, intergranular dissolved pores, and intragranular dissolved pores. The total number of pores obtained from the point counting of the digital images of thin sections with the software Jmicrovision.

Figure 6 Statistics on physical properties of different lithofacies types: (a) The max porosity, min porosity, and average porosity of nine types of lithofacies; and (b) The max permeability, min permeability, and average permeability of nine types of lithofacies. N-total number of samples. The data of porosity of different lithofaices (i.e., max, min, and average values of porosity of each lithofacies) obtained from 82 samples in Figure 6a. The data of permeability of different lithofacies (i.e., max, min, and average values of permeability of each lithofacies) obtained from 73 samples in Figure 6b.

Figure 7 Statistics on physical properties of different lithofacies types within medium-grained

sandstones and fine-grained sandstones and statistics on physical properties of sandstones with different grain size and the same bedding: (a)-(b) Statistics on physical properties of different lithofacies types within medium-grained sandstones and fine-grained sandstones, (a) Medium-grained sandstones, (b) Fine-grained sandstones; (c)-(f) Statistics on physical properties of sandstones with different grain size and the same bedding, (c) Large tabular cross bedding, (d) Small tabular cross bedding, (e) Massive bedding, (f) Parallel bedding and horizontal bedding. N-total number of samples.

Figure 8 The schematic diagram of a relationship among energy of sedimentary environment, bedform, and bedding (Harms and Fahnestoek, 1965; Simons et al., 1965).

Figure 9 The relationship between channel sinuosity and slope (Kneller, 2003). Note: β-The angle of slope, $\beta 1 > \beta 2$.

Figure 10 The schematic diagram of a relationship between energy of sedimentary environment and grain size: (a) A relationship between grain size and current velocity during the deposition, transportation, and erosion; (b) A relationship between grain size and current velocity; (c) Well J14, the cumulative percentage curve of grain size of sandstones; (d) Well J14, the logging column; (e) Well G2, the cumulative percentage curve of grain size of sandstones; and (f) Well G2, the logging column.

Figure 11 The relationship between grain sorting coefficient and D50, compaction rate of different lithofacies types: (a) A relationship between grain sorting of sandstones and compaction; and (b) The cross-plot of D50 and So in different lithofacies types, statistics on average values of D50 and So. So-grain sorting coefficient, C_{rate}-compaction rate, and D50-median grain size. N-total number of samples. The data of cross-plot of So-C_{rate} obtained

from average values of So and C_{rate} of each lithofacies from Table 2. The data of D50 and So of different lithofacies (i.e., average values of D50 and So of different lithofacies) obtained from 65 samples in Figure 11b.

Figure 12 The relationship among compositional maturity, early compaction, and dissolution: (a) The relationship between compositional maturity and dissolution; and (b) The relationship between early compaction and dissolution. C_{rate}-compaction rate, D_{rate}-dissolution rate, C_m-compositional maturity. The data of cross-plot of D_{rate}-C_m obtained from average values of D_{rate} and C_m of each lithofacies from Table 2. The data of cross-plot of D_{rate}-C_{rate} obtained from average values of D_{rate} and C_{rate} of each lithofacies from Table 2.

Figure 13 The quartz-quartz / (feldspar + rock fragments) cross-plot chart of different lithofacies. Note: N- total number of samples. The compositional maturity of sandstones is reflected by the content of quartz and siliciclast (Taylor et al., 2010).

Figure 14 The diagrams show the relationship among the coefficient of skewness, mean coefficient, and median pore-throat radius, and the statistics of the physical property difference of each original lithofacies in different lithofacies assemblies: (a) The cross-plot of porosity and permeability of massive bedded medium-grained sandstones in the assembly of massive bedded lithofacies + tabular cross bedded lithofacies and the assembly of massive bedded lithofacies + parallel bedded lithofacies, respectively; (b) The cross-plot of porosity and permeability of tabular cross bedded medium-grained sandstones in the assembly of massive bedded lithofacies + tabular cross bedded lithofacies and the assembly of tabular cross bedded lithofacies + parallel bedded lithofacies, respectively; (c) The cross-plot of porosity and permeability of parallel bedded medium-grained sandstones in the assembly of

massive bedded lithofacies + parallel bedded lithofacies and the assembly of tabular cross bedded lithofacies + parallel bedded lithofacies, respectively; (d) The cross-plot of porosity and permeability of massive bedded fine-grained sandstones in the assembly of massive bedded lithofacies + tabular cross bedded lithofacies and the assembly of massive bedded lithofacies + parallel bedded lithofacies + horizontal bedded lithofacies, respectively; (e) The cross-plot of porosity and permeability of parallel bedded fine-grained sandstones in the assembly of massive bedded lithofacies + parallel bedded lithofacies, the assembly of tabular cross bedded lithofacies + parallel bedded lithofacies, and the assembly of massive bedded lithofacies + parallel bedded lithofacies + horizontal bedded lithofacies, respectively; and (f) The cross-plot chart of coefficient of skewness and median pore-throat radius of the assembly of massive bedded lithofacies + tabular cross bedded lithofacies and the assembly of tabular cross bedded lithofacies + parallel bedded lithofacies. Note: N-total number of samples.

Figure 15 The diagrams show the relationship among the dissolution, compaction, grain sorting, and compositional maturity of sandstones in different lithofacies assemblies: (a) The D_{rate}-So cross-plot chart of massive bedded lithofacies in the assembly of massive bedded lithofacies + tabular bedded lithofacies, the assembly of massive bedded lithofacies + parallel bedded lithofacies, and the assembly of massive bedded lithofacies + parallel bedded lithofacies + horizontal bedded lithofacies, respectively; (b) The quartz-quartz / (feldspar + rock fragments) cross-plot chart of tabular cross bedded lithofacies in the assembly of massive bedded lithofacies + tabular cross bedded lithofacies and the assembly of tabular cross bedded lithofacies + parallel bedded lithofacies, respectively; and (c) The C_{rate} of different lithofacies assembly types. D_{rate}-dissolution rate, So-grain sorting coefficient,

903 C_{rate}-compaction rate. N-total number of samples.

904 **Figure 16** The schematic diagram shows the differential diagenesis controls on the physical

905 properties of lithofacies in sandstone reservoirs.

Table 1(a) The testing information of samples from the Jurassic Shaximiao Formation of the eastern slope in western Sichuan depression

Type of experiment	Physical properties		Thin section identification data				Mercury injection	
	Porosity	Permeability	Grain size	Components (quartz / feldspar / rock fragments)	Photos (pore structure)	Pore diameter	Median pore-throat radius	Capillary pressure curve
M	26	23	10	10	5	4	13	7
N	82	73	65	80	/	42	88	8

Note: The sign of "/"means that there is no measured data in these wells. M-total number of individual wells; N-total number of real analyzed samples.

Table 1(b) The sampling depth of physical property measurement from the Jurassic Shaximiao Formation of the eastern slope in western Sichuan depression

Well	G1	G2	G3	G4	G5	G6	G7	G8
Porosity	3174.35-3177.78, 3170.9-3175.26	2580.52-2583.34, 2583.16-2588.09, 2716.15-2718.48, 2719.7-2724.49, 3036.61-3040.93, 3040.73-3044.41	2814.47-2819.43	2397.76-2401.5	2291.85-2298.78, 2586.54-2593.37	2359.74-2363.17, 2365.53-2368.8	2895.53-2899.95, 2899.05-2899.48	2834.53-2842.18, 2871.8-2873.67
Permeability	3174.35-3177.78, 3170.9-3175.26	2580.52-2583.34, 2583.16-2588.09, 2716.15-2718.48, 2719.7-2724.49, 3036.61-3040.93, 3040.73-3044.41	2814.47-2819.43	2397.76-2401.5	2291.85-2298.78, 2586.54-2593.37	2359.74-2363.17, 2365.53-2368.8	2895.53-2899.95, 2899.05-2899.48	2834.53-2842.18, 2871.8-2873.67

Note: The sign of "/"means that there is no measured data in these wells. The unit of the sampling depth is "meter".

Table 1(b) Continued

Well	G9	G11	G12	G13	G14	J1	J2	J3
Porosity	2847.5-2851.9, 2912.3-2918.1	2767.32-2775.07	2819-2824	2757.17-2762.31, 3188.94-3196.75	2261.58-2268.08, 2608.07-2613.04	2667.27-2673.68, 2673.68-2674.86	2249.94-2252.35, 2328.98-2329.48, 2335.04-2338.43	2177.61-2186.56，2394.35-2395.83，2469.96-2475.08
Permeability	/	2767.32-2775.07	/	2757.17-2762.31, 3188.94-3196.75	2261.58-2268.08, 2608.07-2613.04	2667.27-2673.68, 2673.68-2674.86	2249.94-2252.35, 2328.98-2329.48, 2335.04-2338.43	2177.61-2186.56，2394.35-2395.83，2469.96-2475.08

Note: The sign of “/”means that there is no measured data in these wells. The unit of the sampling depth is “meter”.

Table 1(b) Continued

Well	J4	J6	J7	J8	J9	J10	J11	J12	J13	J14
Porosity	1955.2-1972.2, 2385.49-2394.6	2293.04-2309.51	2141.11-2141.86, 2326.81-2342.07	2045.7-2048.66	1969-1972.76, 1973.03-1979.17, 1979.47-1985.88	1982.79-1997.48	2644.29-2659.99, 2656.57-2659.99	2661.75-2667.67	2161.84-2164.56	2590.9-2598.7, 2598.95-2603.73, 2603.73-2608.68, 2608.68-2613.52
Permeability	1955.2-1972.2, 2385.49-2394.6	2293.04-2309.51	2141.11-2141.86, 2326.81-2342.07	2045.7-2048.66	1969-1972.76, 1973.03-1979.17, 1979.47-1985.88	1982.79-1997.48	2644.29-2659.99, 2656.57-2659.99	/	2161.84-2164.56	2590.9-2598.7, 2598.95-2603.73, 2603.73-2608.68, 2608.68-2613.52

Note: The sign of “/”means that there is no measured data in these wells. The unit of the sampling depth is “meter”.

Table 1(c) The sampling depth of grain size and components measurement from the Jurassic Shaximiao Formation of the eastern slope in western Sichuan depression

Well	G1	G2	G3	G4	G8	G11	G12	J1	J12	J14
Grain size	3170.9-3175.26, 3174.35-3177.78	2582.4-2583.34, 3036.61-3040.93, 3040.73-3044.41	2814.47-2819.43	2397.76-2401.5	2834.53-2842.18, 2871.8-2873.67	2767.32-2775.07	2819-2824	2667.27-2673.68, 2673.68-2674.86	2661.75-2667.67	2590.9-2598.7
Components (quartz / feldspar / rock fragments)	3170.9-3175.26, 3174.35-3177.78	2582.4-2583.34, 3036.61-3040.93, 3040.73-3044.41	2814.47-2819.43	2397.76-2401.5	2834.53-2842.18, 2871.8-2873.67	2767.32-2775.07	2819-2824	2667.27-2673.68, 2673.68-2674.86	2661.75-2667.67	2590.9-2598.7

Note: The unit of the sampling depth is “meter”.

Table 1(d) The sampling depth of photos of pore structure observation and pore diameter measurement from the Jurassic Shaximiao Formation of the eastern slope in western Sichuan depression

Well	G1	G9	G11	J11	J14
Photos (pore structure)	3170.9-3170.93	2848.35-2848.38	2768.17	2649.64, 2656.77	2595.745, 2606.585, 2608.935
Pore diameter	/	2848.35-2851.82, 2913.27-2913.3, 2915.16-2915.19	2767.53-2775.07	2644.06-2649.64, 2656.77-2659.79	2592.745-2598.715, 2608.935

Note: The sign of “/”means that there is no measured data in these wells. The unit of the sampling depth is “meter”.

Table 1(e) The sampling depth of photos of median pore-throat radius and capillary pressure curve measurement from the Jurassic Shaximiao Formation of the eastern slope in western Sichuan depression

Well	G3	G7	G11	G14	J1	J2	J4	J7	J9	J10	J11	J13	J14
Median pore-throat radius	2818.2-2814.47	2895.33-2898.22	2767.78-2774.9	2261.58-2268.08	2667.1-2673.68	2249.5-2251.63	1956.9-1967.45	2141.86	1979.66-1985.65	1982.79-1997.48	2645.41-2659.24	2162.28-2163.83	2593.36-2598.11, 2609.84-2609.87
Capillary pressure curve	2818.2	/	2770.97	/	2673.68	2250.42	/	2141.86	/	/	2658.77-2658.80, 2659.21-2659.24	/	2593.36-2593.39

Note: The sign of “/”means that there is no measured data in these wells. The unit of the sampling depth is “meter”.

Table 2 Statistics on the grain sorting coefficient, compositional maturity, primary porosity, compaction rate, dissolution rate, the volume of primary pores, and the volume of dissolved pores of different lithofacies

Lithofacies	Grain sorting coefficient ($\frac{Min\sim Max}{Average}$)	Compositional maturity A ($\frac{Min\sim Max}{Average}$)	Compositional maturity B ($\frac{Min\sim Max}{Average}$)	Φ_0 ($\frac{Min\sim Max}{Average}$)	V_i	V_m	V_c	C_{rate}	D_{rate}	The volume of primary pores	The volume of dissolved pores
S_{mm}	$\frac{1.47\sim1.56}{1.51}$	$\frac{0.58\sim1.74}{1.18}$	$\frac{0.59\sim1.86}{1.23}$	$\frac{35.59\%\sim36.49\%}{36.08\%}$	6.00%	1.00%	3.00%	72.28%	16.63%	26.67%	6.00%
S_{mf}	$\frac{1.45\sim1.7}{1.53}$			$\frac{34.38\%\sim36.70\%}{35.88\%}$	3.00%	2.00%	5.00%	72.13%	8.36%	26.59%	3.00%
S_{ltm}	$\frac{1.45\sim1.67}{1.58}$	$\frac{0.54\sim1.52}{0.90}$	$\frac{0.56\sim1.56}{0.94}$	$\frac{34.62\%\sim36.70\%}{35.40\%}$	4.00%	1.00%	4.00%	74.58%	11.30%	26.05%	4.00%
S_{ltf}	$\frac{1.47\sim1.84}{1.59}$			$\frac{33.36\%\sim36.49\%}{35.31\%}$	3.00%	2.00%	3.00%	77.34%	8.50%	25.67%	3.00%
S_{stm}	$\frac{1.47\sim1.71}{1.6}$	$\frac{0.61\sim1.14}{0.77}$	$\frac{0.61\sim1.44}{0.94}$	$\frac{34.30\%\sim36.49\%}{35.31\%}$	3.00%	3.00%	1.00%	80.18%	8.50%	25.31%	3.00%
S_{stf}	$\frac{1.45\sim1.71}{1.63}$			$\frac{34.30\%\sim36.70\%}{35.31\%}$	3.00%	2.00%	1.00%	83.01%	8.50%	24.96%	3.00%
S_{pm}	$\frac{1.63\sim1.67}{1.65}$	$\frac{0.42\sim1.28}{0.68}$	$\frac{0.43\sim1.33}{0.82}$	$\frac{34.62\%\sim34.96\%}{34.79\%}$	2.00%	1.00%	3.00%	82.75%	5.75%	24.77%	2.00%
S_{pf}	$\frac{1.63\sim1.84}{1.67}$			$\frac{33.36\%\sim34.96\%}{34.62\%}$	2.00%	2.00%	2.00%	82.67%	5.78%	24.71%	2.00%
S_{hf}	$\frac{1.7\sim1.83}{1.72}$	$\frac{0.42\sim0.74}{0.51}$	$\frac{0.43\sim0.75}{0.52}$	$\frac{33.42\%\sim34.38\%}{34.22\%}$	2.00%	2.00%	0.00%	88.31%	5.84%	23.88%	2.00%

Note: $\emptyset_0$- primary porosity; V_i-the volume of intergranular pores (average vaules); V_c-the volume of cements (average values); V_m-the volume of matrix (average values); C_{rate}-compaction rate (average values); D_{rate}-dissolution rate (average values). The volume of primary pores and the volume of dissolved pores-average values. S_{ltm}-large tabular cross bedded medium-grained sandstone; S_{stm}-small tabular cross bedded medium-grained sandstone; S_{ltf}-large tabular cross bedded fine-grained sandstone; S_{stf}-small tabular cross bedded fine-grained sandstone; S_{mm}-massive bedded medium-grained sandstone; S_{mf}-massive bedded fine-grained sandstone; S_{pm}-parallel bedded medium-grained sandstone; S_{pf}-parallel bedded fine-grained sandstone; S_{hf}-horizontal bedding fine-grained sandstone. The data of compositional maturity A were calculated after the unstable minerals affected by the weathering previous the beginning of transport, and the data of compositional maturity B were calculated after later burial diagenesis.

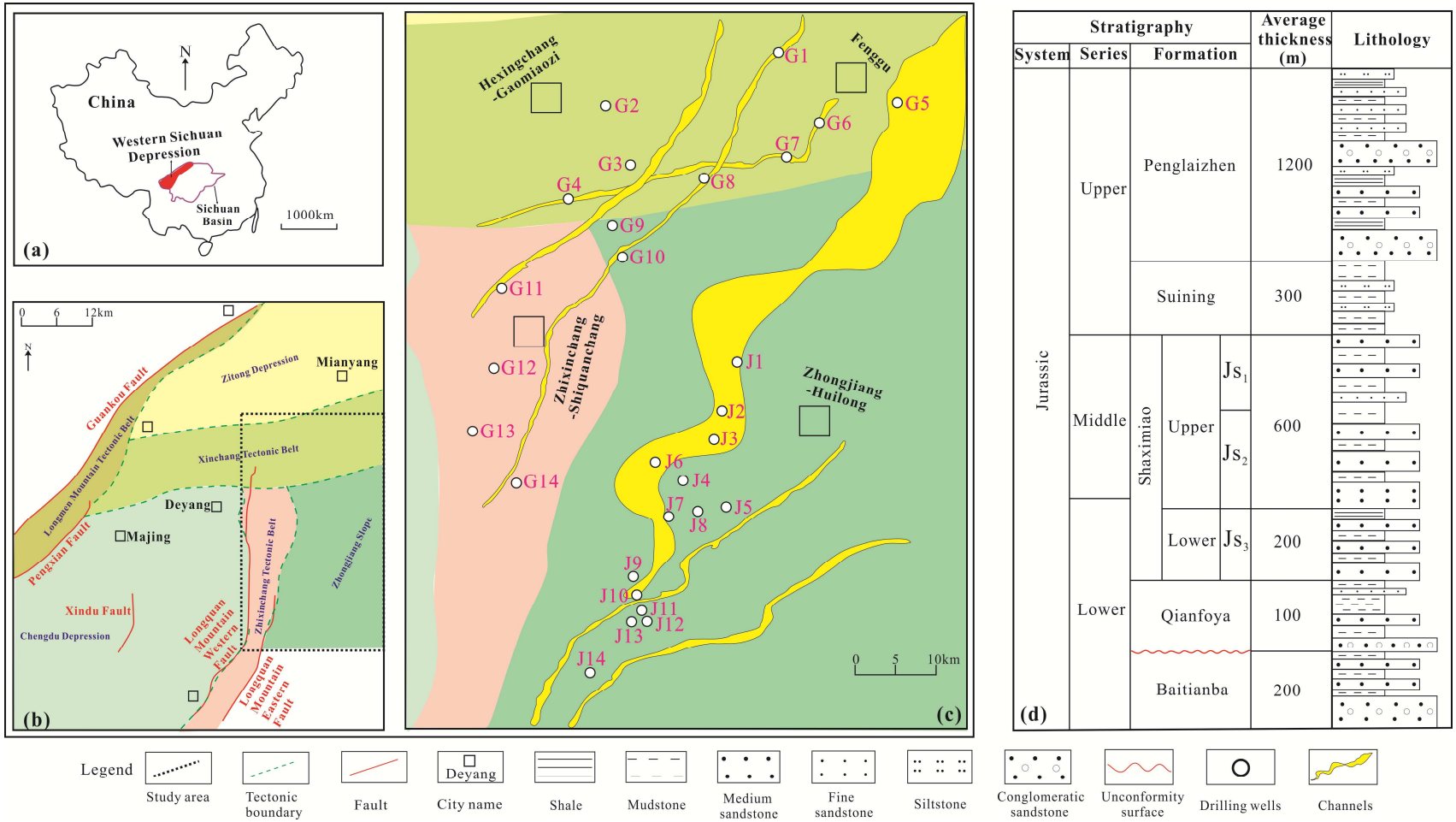

Figure 1 The location of the eastern slope of western Sichuan depression and the stratigraphic column of the Jurassic Shaximiao Formation (Liu et al., 2018): (a) The location of the western Sichuan depression in Sichuan Basin; (b) The map shows that six tectonic zones of the western Sichuan depression and tectonic subzones developed in the study area; (c) The locations of 28 cored wells; and (d) The stratigraphic column of the Jurassic Shaximiao Formation in the study area. The Upper Shaximiao Formation is divided into Js_1 and Js_2, and the Lower Shaximiao Formation is named by Js_3.There are straight channels and sinuous channels with the dispersing sandbodies developing in the study area as shown in Figure1c, and the channels shown in this figure developed in Js_1^4 sand group and $Js_3^{3\text{-}2}$ sand group of the study area.

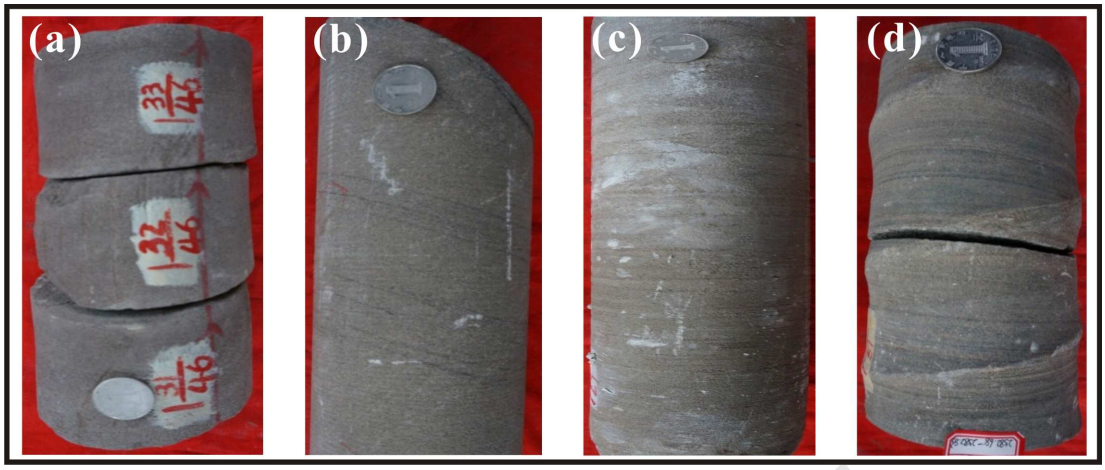

Figure 2 Photos of sandstones with different sedimentary bedding: (a) Well J12, depth: 2665.55-2665.85m, massive bedding; (b) Well G14, depth: 2818.24-2818.56m, tabular cross bedding; (c) Well G11, depth: 2773.22-2773.62m, parallel bedding; and (d) Well G2, depth: 2582.68-2582.83, horizontal bedding.

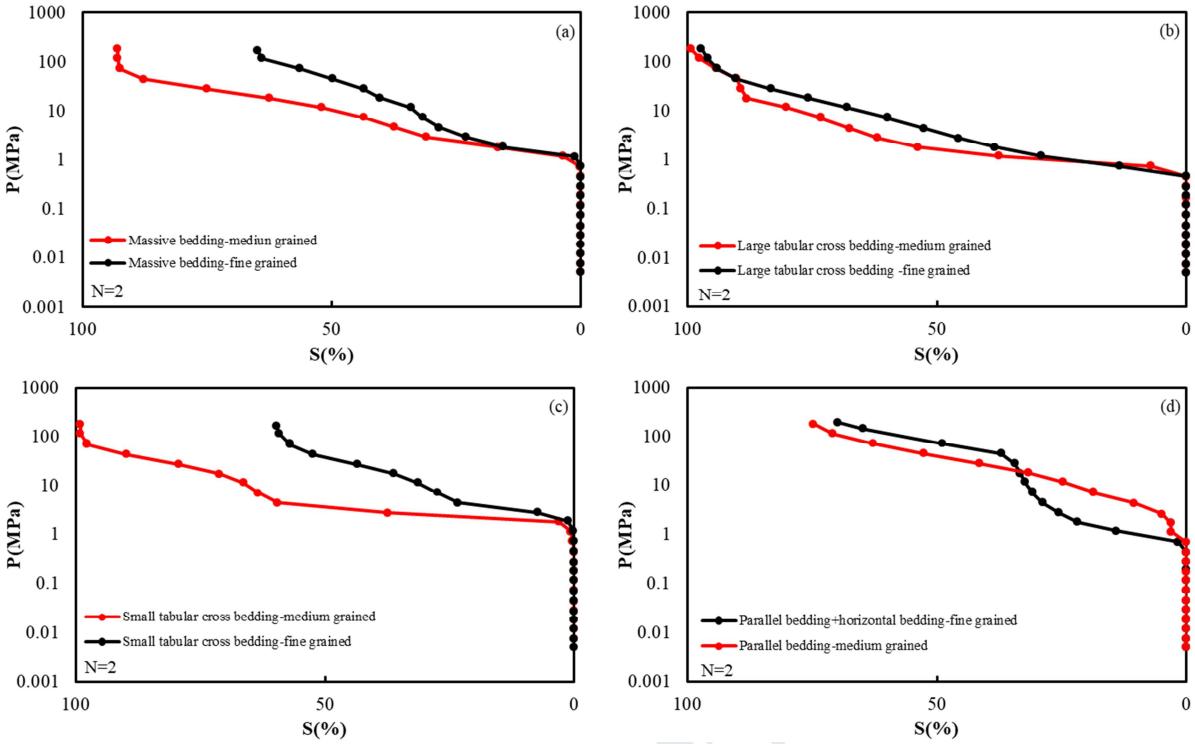

Figure 3 The Cross-plot of the applied mercury pressure versus the incremental mercury saturation indicating capillary injection curves of different lithofacies: (a) Capillary injection curves of massive bedded sandstones; (b) Capillary injection curves of large tabular cross bedded sandstones; (c) Capillary injection curves of small tabular cross bedded sandstones; and (d) Capillary injection curves of parallel bedded sandstones and horizontal bedded sandstones. P-applied mercury pressure; S-incremental mercury saturation; N-total number of samples. The data of capillary injection curves of different lithofacies obtained from 8 samples of 7 cored wells in total.

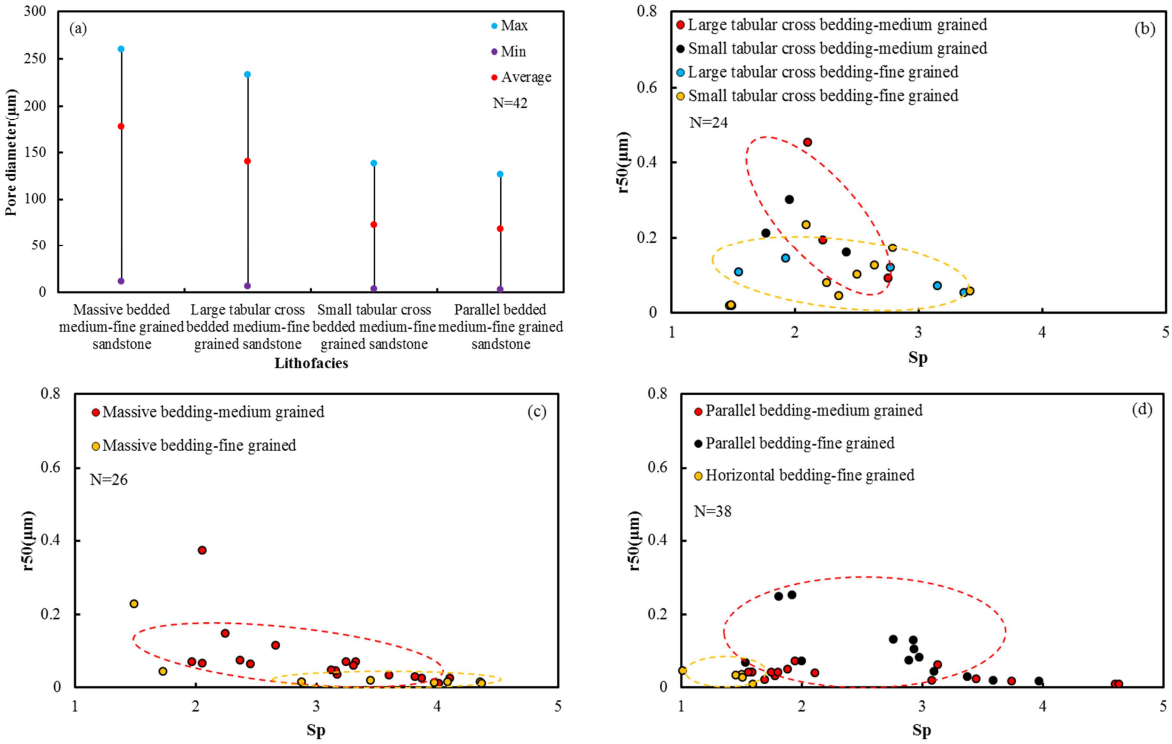

Figure 4 Statistics on the pore diameter of different lithofacies types and r50-Sp cross-plots of the different grain size of sandstones with the same bedding: (a) Statistics on the pore diameter of different lithofacies; (b)-(d) r50-Sp cross-plots of different grain size of sandstones with the same bedding, (b) Large/small tabular cross bedded sandstones, (c) Massive bedded sandstones, and (d) Parallel bedded sandstones and horizontal bedded sandstones. r50-median pore-throat radius. Sp-pore sorting coefficient. The red circle refers to the medium-grained lithofacies, and the yellow circle refers to the fine-grained lithofacies. N-total number of samples. The data of pore diameter of different lithofacies (i.e., max, min, and average values of pore diameter of each lithofacies) obtained from 42 samples in Figure 4a.

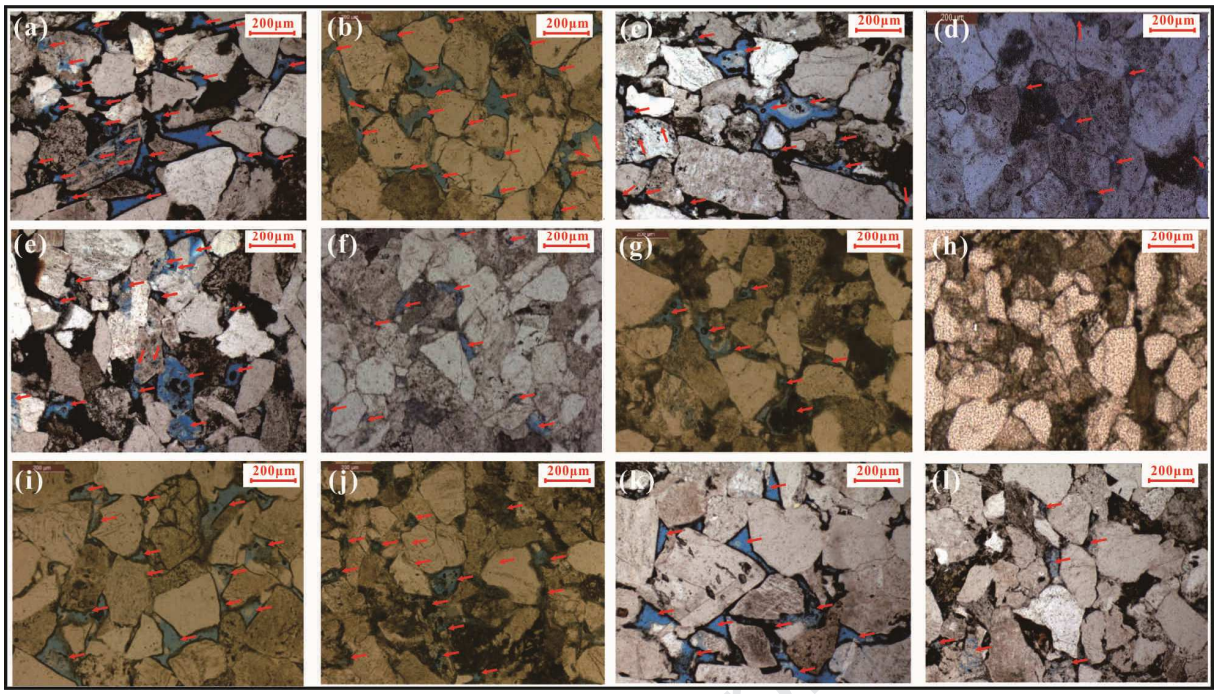

Figure 5 Thin section photos show pore structure of different lithofacies types: (a) Well J14, depth: 2606.585m, massive bedded medium-grained sandstone, total number of pores-708; (b) Well J11, 2656.77m, large tabular cross bedded medium-grained sandstone, total number of pores-783; (c) Well J14, 2595.745m, small tabular cross bedded medium-grained sandstone, total number of pores-532; (d) Well G11, 2768.17m, parallel bedded medium-grained sandstone, total number of pores-231; (e) Well J14, 2608.935m, massive bedded fine-grained sandstone, total number of pores-362; (f) Well G9, 2848.35-2848.38m, large tabular cross bedded fine-grained sandstone, total number of pores-95; (g) Well J11, 2649.64m, small tabular cross bedded fine-grained sandstone, total number of pores-306; and (h) Well G1, 3170.9 -3170.93m, parallel bedded fine-grained sandstone, no pores. (i) Well J11, 2654.16mm, tabular cross bedded medium-grained sandstone in the lithofacies assembly with massive bedded lithofacies, total number of pores-609, the pore type is composed of intergranular pores, good pore connectivity can be seen in this figure; (j) Well J11, 2654.99 mm, tabular cross bedded medium-grained sandstone in the lithofacies assembly with parallel bedded lithofacies, total number of pores-604, the pore type is composed of intergranular dissolved pores, poor pore connectivity can be seen in this figure; (k) Well J14, 2608.065 mm, parallel bedded fine-grained sandstone in the assembly of massive bedded lithofacies + parallel bedded lithofacies, total number of pores-294, the pore type is composed of intergranular dissolved pores and intergranular dissolved pores, poor pore connectivity can be seen in this figure; (l) Well J14, 2608.485 mm, parallel bedded fine-grained sandstone in the assembly of massive bedded lithofacies + parallel bedded lithofacies +horizontal bedded lithofacies, a few of pores and poor pore connectivity can be seen in this figure. Red arrow refers to the intergranular pores, intergranular dissolved pores, and intragranular dissolved pores. The total number of pores obtained from the point counting of the digital images of thin sections with the software Jmicrovision.

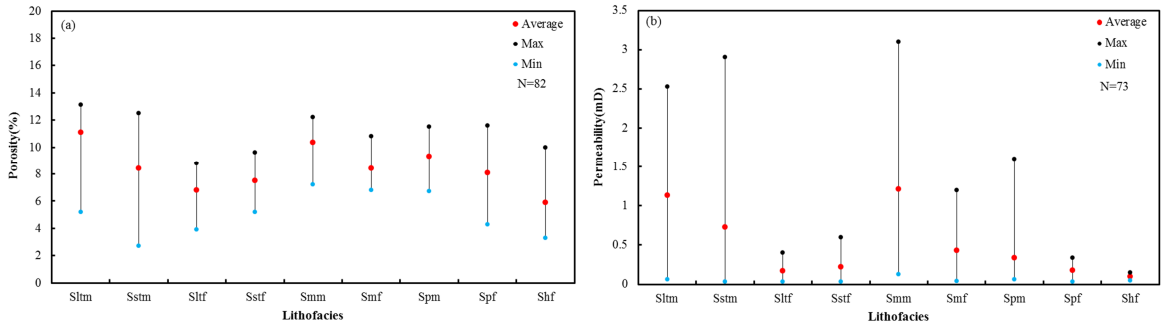

Figure 6 Statistics on physical properties of different lithofacies types: (a) The max porosity, min porosity, and average porosity of nine types of lithofacies; and (b) The max permeability, min permeability, and average permeability of nine types of lithofacies. N-total number of samples. The data of porosity of different lithofaices (i.e., max, min, and average values of porosity of each lithofacies) obtained from 82 samples in Figure 6a. The data of permeability of different lithofacies (i.e., max, min, and average values of permeability of each lithofacies) obtained from 73 samples in Figure 6b.

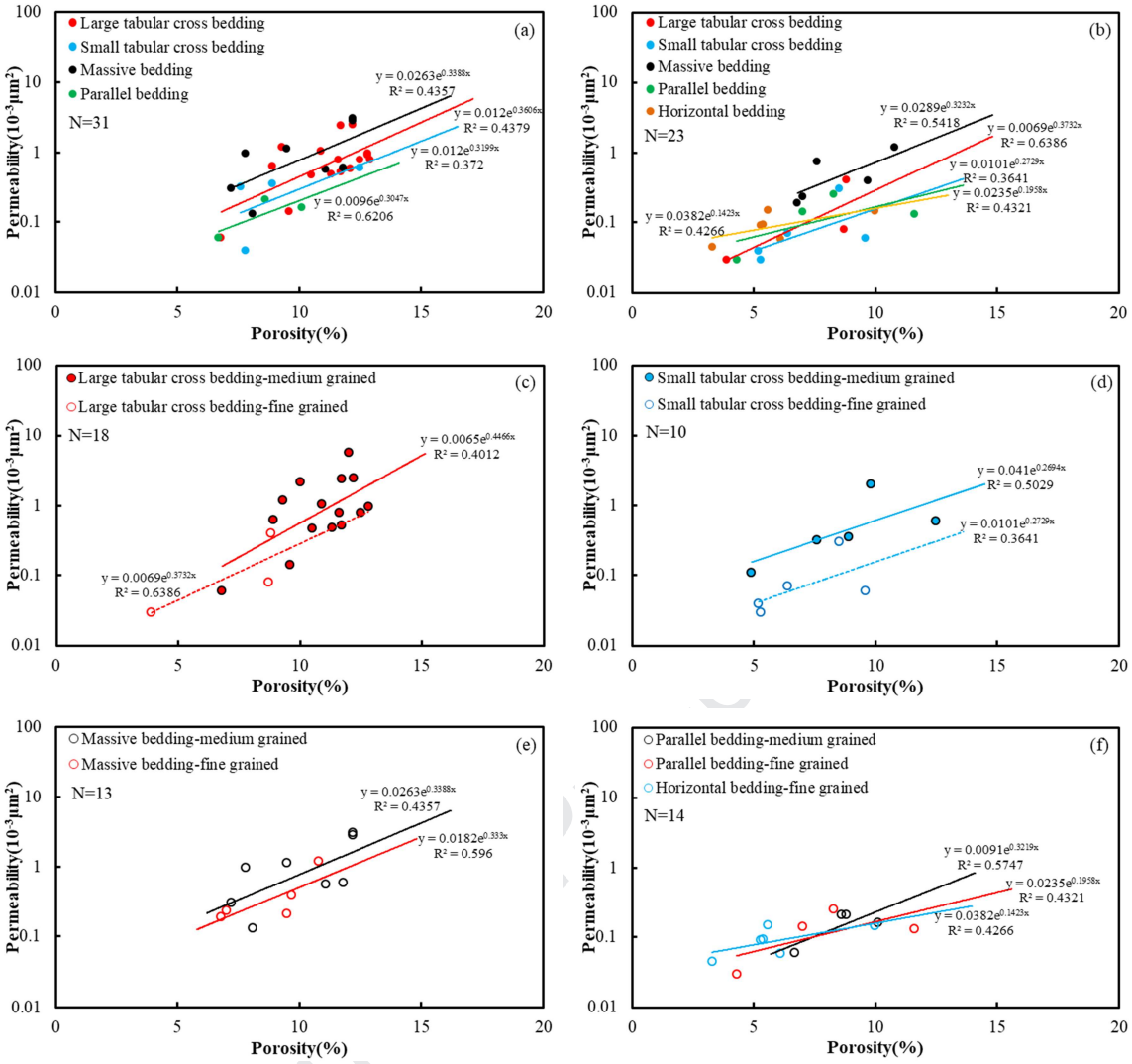

Figure 7 Statistics on physical properties of different lithofacies types within medium-grained sandstones and fine-grained sandstones and statistics on physical properties of sandstones with different grain size and the same bedding: (a)-(b) Statistics on physical properties of different lithofacies types within medium-grained sandstones and fine-grained sandstones, (a) Medium-grained sandstones, (b) Fine-grained sandstones; (c)-(f) Statistics on physical properties of sandstones with different grain size and the same bedding, (c) Large tabular cross bedding, (d) Small tabular cross bedding, (e) Massive bedding, (f) Parallel bedding and horizontal bedding. N-total number of samples.

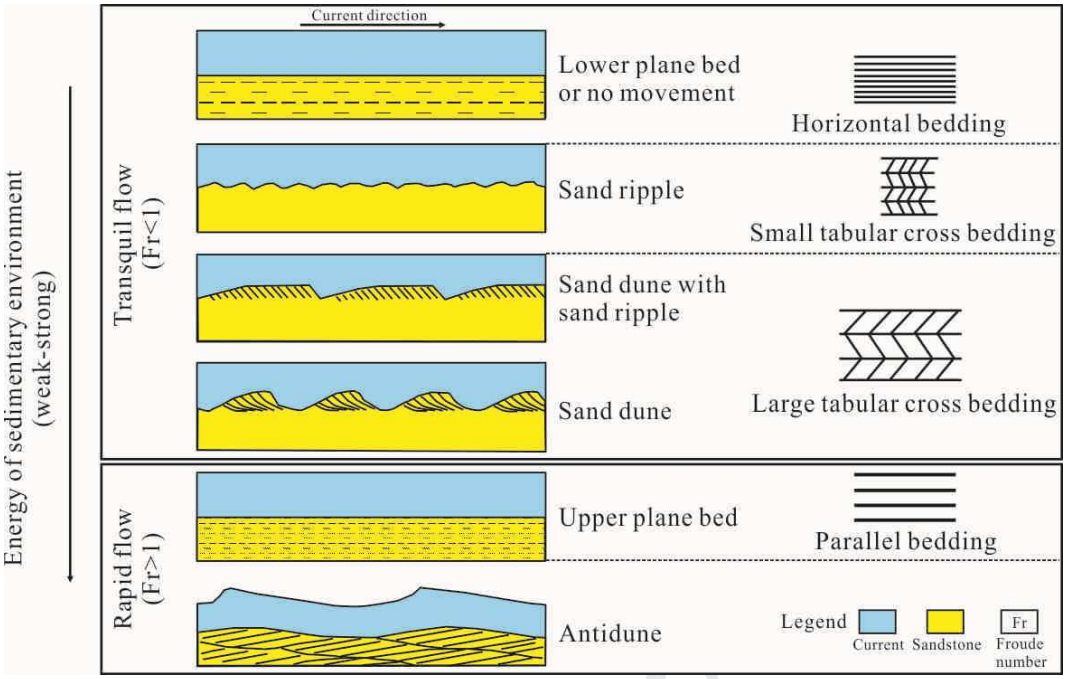

Figure 8 The schematic diagram of a relationship among energy of sedimentary environment, bedform, and bedding (Harms and Fahnestoek, 1965; Simons et al., 1965)

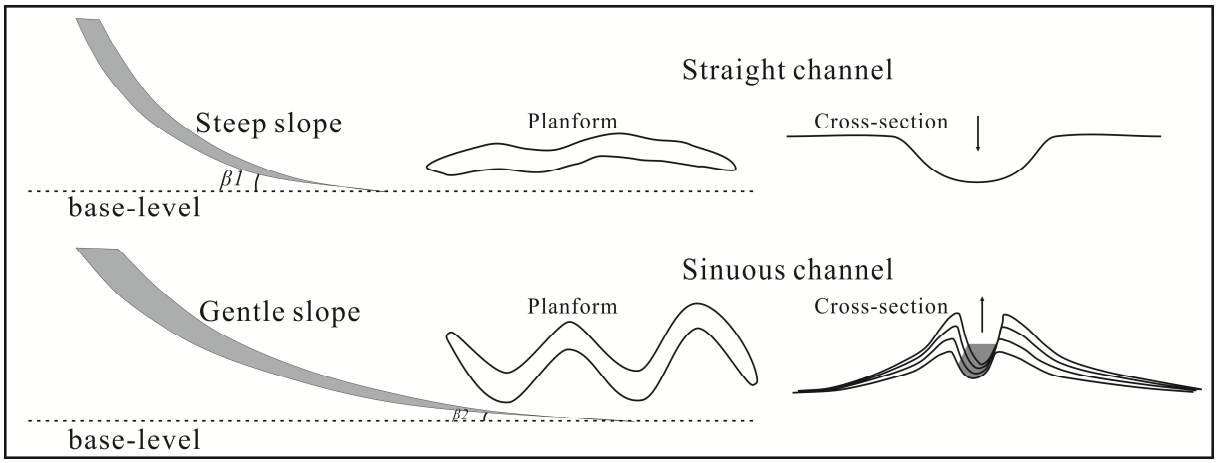

Figure 9 The relationship between channel sinuosity and slope (Kneller, 2003)

Note: β-The angle of slope, $\beta 1 > \beta 2$.

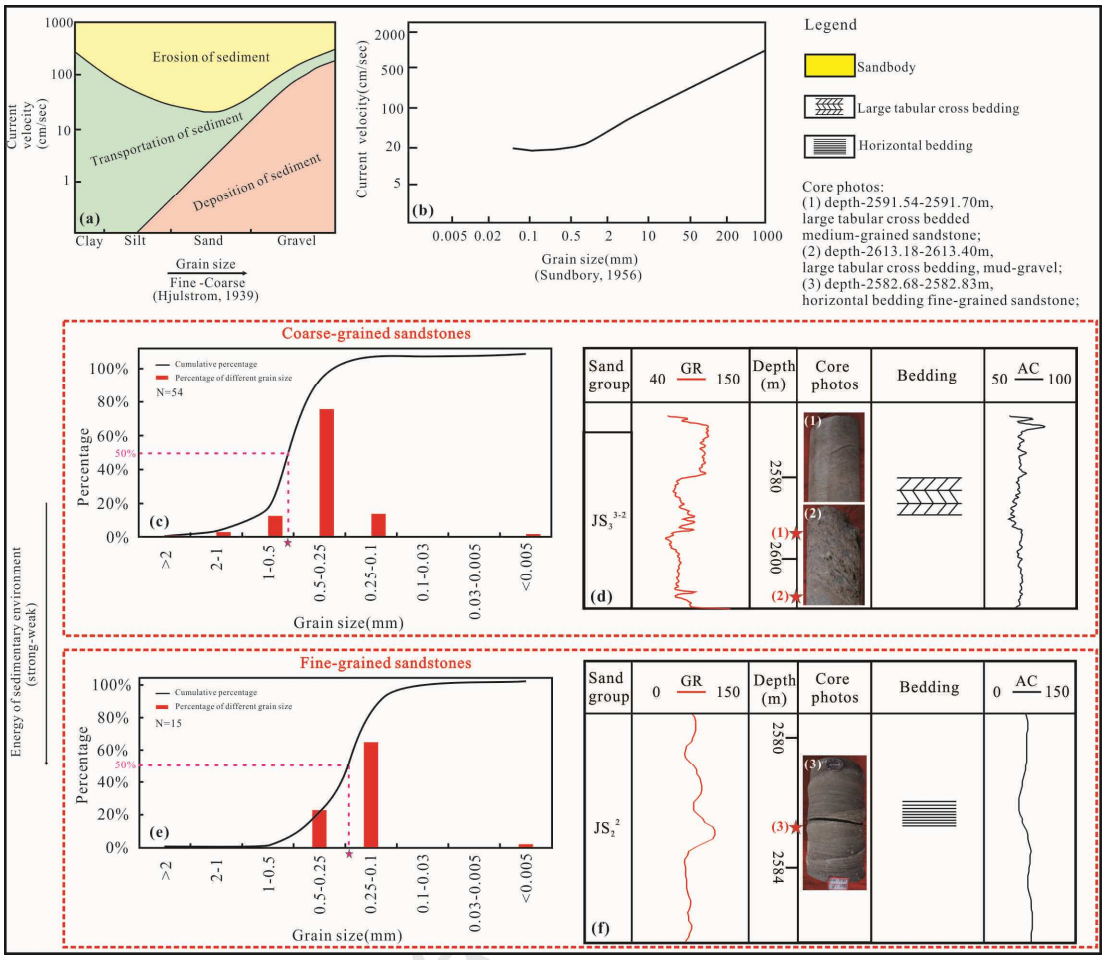

Figure 10 The schematic diagram of a relationship between energy of sedimentary environment and grain size: (a) A relationship between grain size and current velocity during the deposition, transportation, and erosion; (b) A relationship between grain size and current velocity; (c) Well J14, the cumulative percentage curve of grain size of sandstones; (d) Well J14, the logging column; (e) Well G2, the cumulative percentage curve of grain size of sandstones; and (f) Well G2, the logging column.

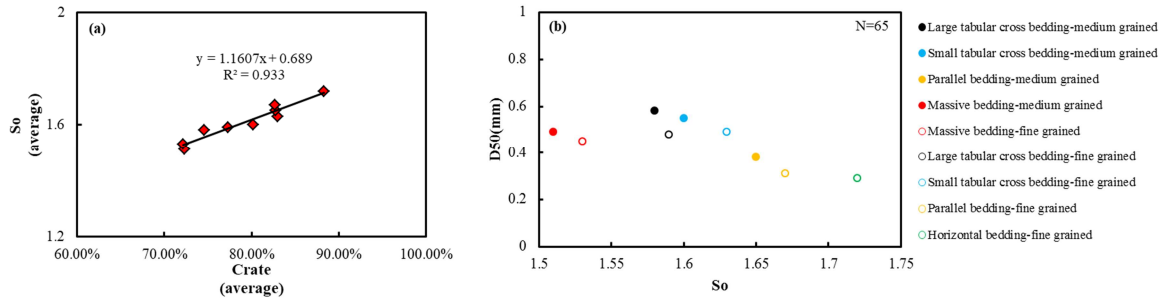

Figure 11 The relationship between grain sorting coefficient and D50, compaction rate of different lithofacies types: (a) A relationship between grain sorting of sandstones and compaction; and (b) The cross-plot of D50 and So in different lithofacies types, statistics on average values of D50 and So. So-grain sorting coefficient, C_{rate}-compaction rate, and D50-median grain size. N-total number of samples. The data of cross-plot of So-C_{rate} obtained from average values of So and C_{rate} of each lithofacies from Table 2. The data of D50 and So of different lithofacies (i.e., average values of D50 and So of different lithofacies) obtained from 65 samples in Figure 11b.

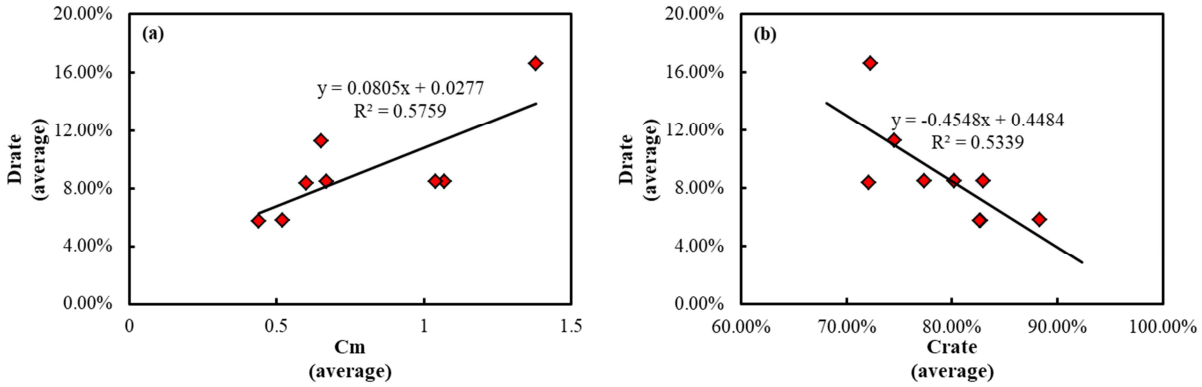

Figure 12 The relationship among compositional maturity, early compaction, and dissolution: (a) The relationship between compositional maturity and dissolution; and (b)The relationship between early compaction and dissolution. C_{rate}-compaction rate, D_{rate}-dissolution rate, C_m-compositional maturity. The data of cross-plot of D_{rate} -C_m obtained from average values of D_{rate} and C_m of each lithofacies from Table 2. The data of cross-plot of D_{rate} –C_{rate} obtained from average values of D_{rate} and C_{rate} of each lithofacies from Table 2.

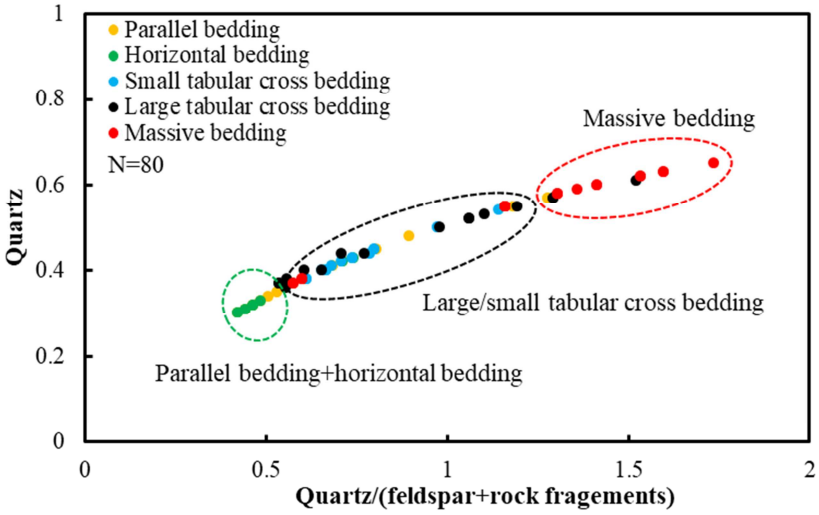

Figure 13 The quartz-quartz / (feldspar + rock fragments) cross-plot chart of different lithofacies
Note: N- total number of samples. The compositional maturity of sandstones is reflected by the content of quartz and siliciclast (Taylor et al., 2010).

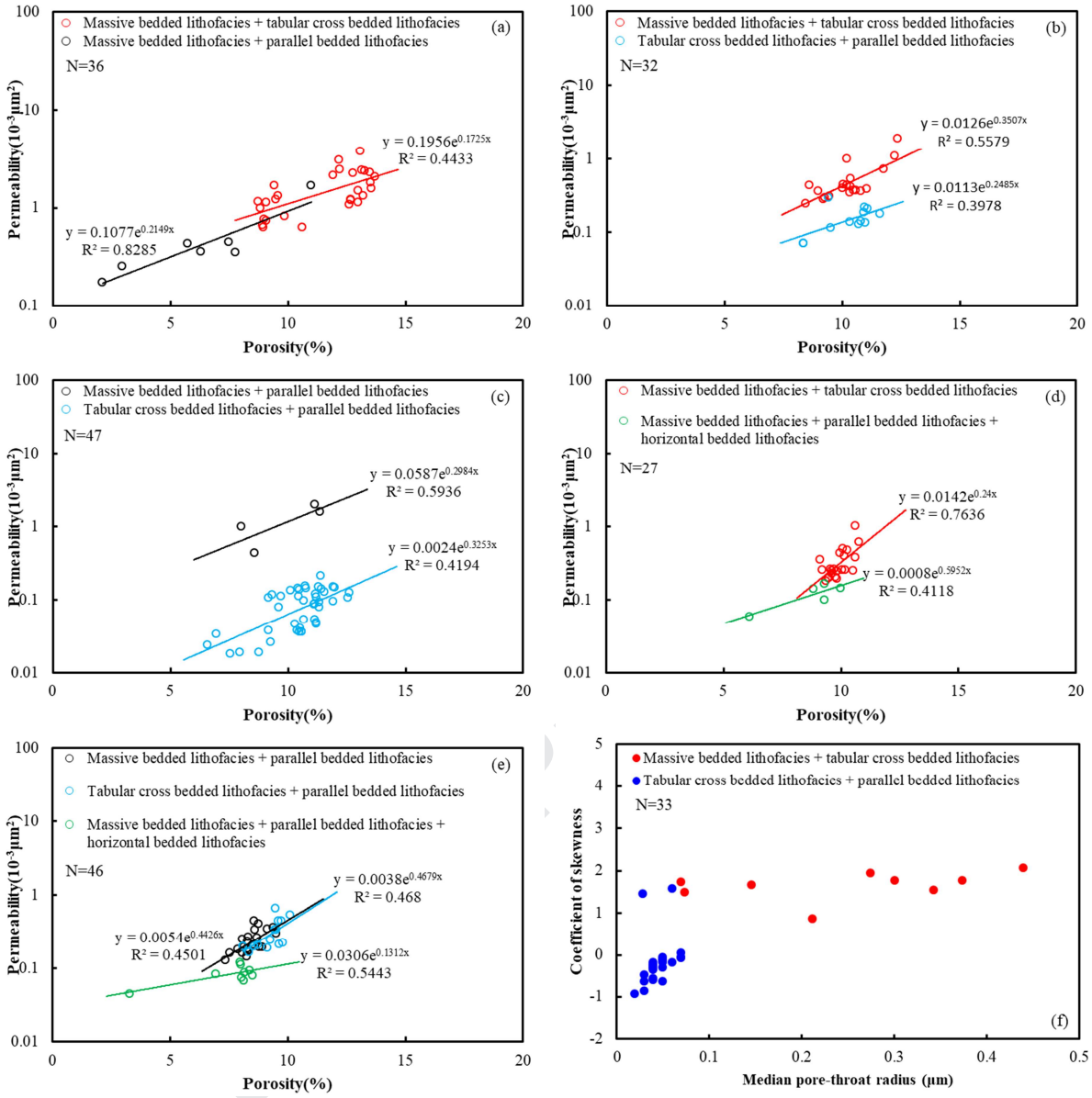

Figure 14 The diagrams show the relationship among the coefficient of skewness, mean coefficient, and median pore-throat radius, and the statistics of the physical property difference of each original lithofacies in different lithofacies assemblies: (a) The cross-plot of porosity and permeability of massive bedded medium-grained sandstones in the assembly of massive bedded lithofacies + tabular cross bedded lithofacies and the assembly of massive bedded lithofacies + parallel bedded lithofacies, respectively; (b) The cross-plot of porosity and permeability of tabular cross bedded medium-grained sandstones in the assembly of massive bedded lithofacies + tabular cross bedded lithofacies and the assembly of tabular cross bedded lithofacies + parallel bedded lithofacies, respectively; (c) The cross-plot of porosity and permeability of parallel bedded medium-grained sandstones in the assembly of massive bedded lithofacies + parallel bedded lithofacies and the assembly of tabular cross bedded lithofacies + parallel bedded lithofacies, respectively; (d) The cross-plot of porosity and permeability of massive bedded fine-grained sandstones in the assembly of massive bedded lithofacies + tabular cross bedded lithofacies and the assembly of massive bedded lithofacies + parallel bedded lithofacies + horizontal bedded lithofacies, respectively; (e) The cross-plot of porosity and permeability of parallel bedded fine-grained sandstones in the assembly of massive bedded lithofacies + parallel bedded lithofacies, the assembly of tabular cross bedded lithofacies + parallel bedded lithofacies, and the assembly of massive bedded lithofacies + parallel

bedded lithofacies + horizontal bedded lithofacies, respectively; and (f) The cross-plot chart of coefficient of skewness and median pore-throat radius of the assembly of massive bedded lithofacies + tabular cross bedded lithofacies and the assembly of tabular cross bedded lithofacies + parallel bedded lithofacies. Note: N-total number of samples.

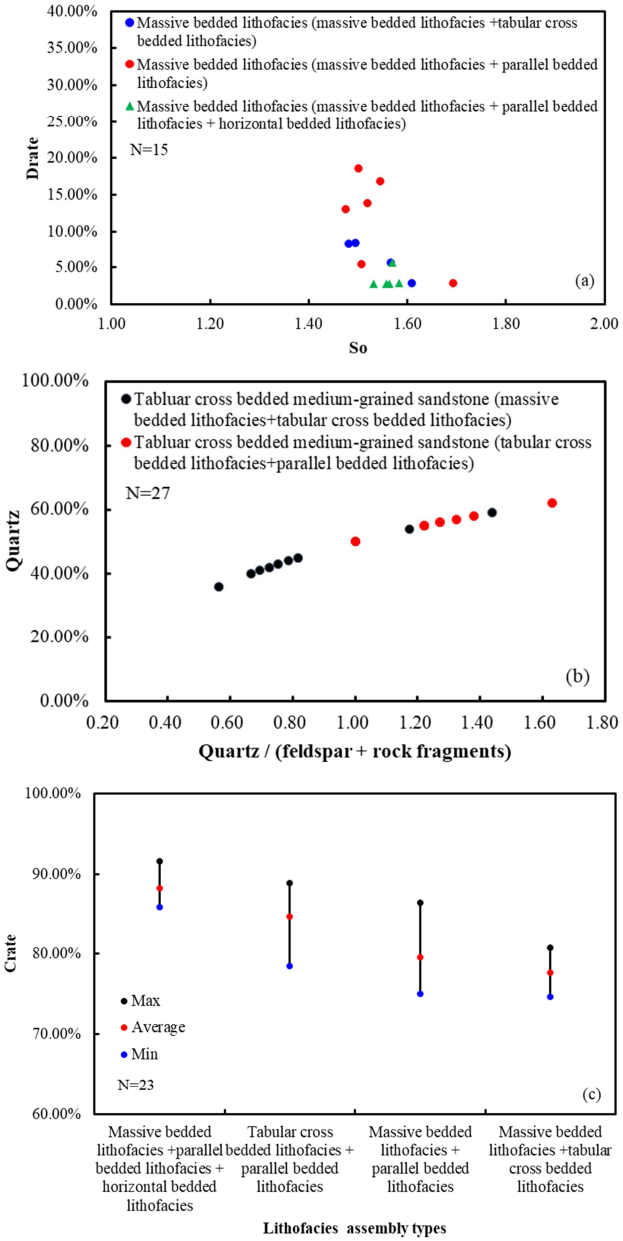

Figure 15 The diagrams show the relationship among the dissolution, compaction, grain sorting, and compositional maturity of sandstones in different lithofacies assemblies: (a) The D_{rate}-So cross-plot chart of massive bedded lithofacies in the assembly of massive bedded lithofacies + tabular bedded lithofacies, the assembly of massive bedded lithofacies + parallel bedded lithofacies, and the assembly of massive bedded lithofacies + parallel bedded lithofacies + horizontal bedded lithofacies, respectively; (b) The quartz-quartz / (feldspar + rock fragments) cross-plot chart of tabular cross bedded lithofacies in the assembly of massive bedded lithofacies + tabular cross bedded lithofacies and the assembly of tabular cross bedded lithofacies + parallel bedded lithofacies, respectively; and (c) The C_{rate} of different lithofacies assembly types. D_{rate}-dissolution rate, So-grain sorting coefficient, C_{rate}-compaction rate. N-total number of samples.

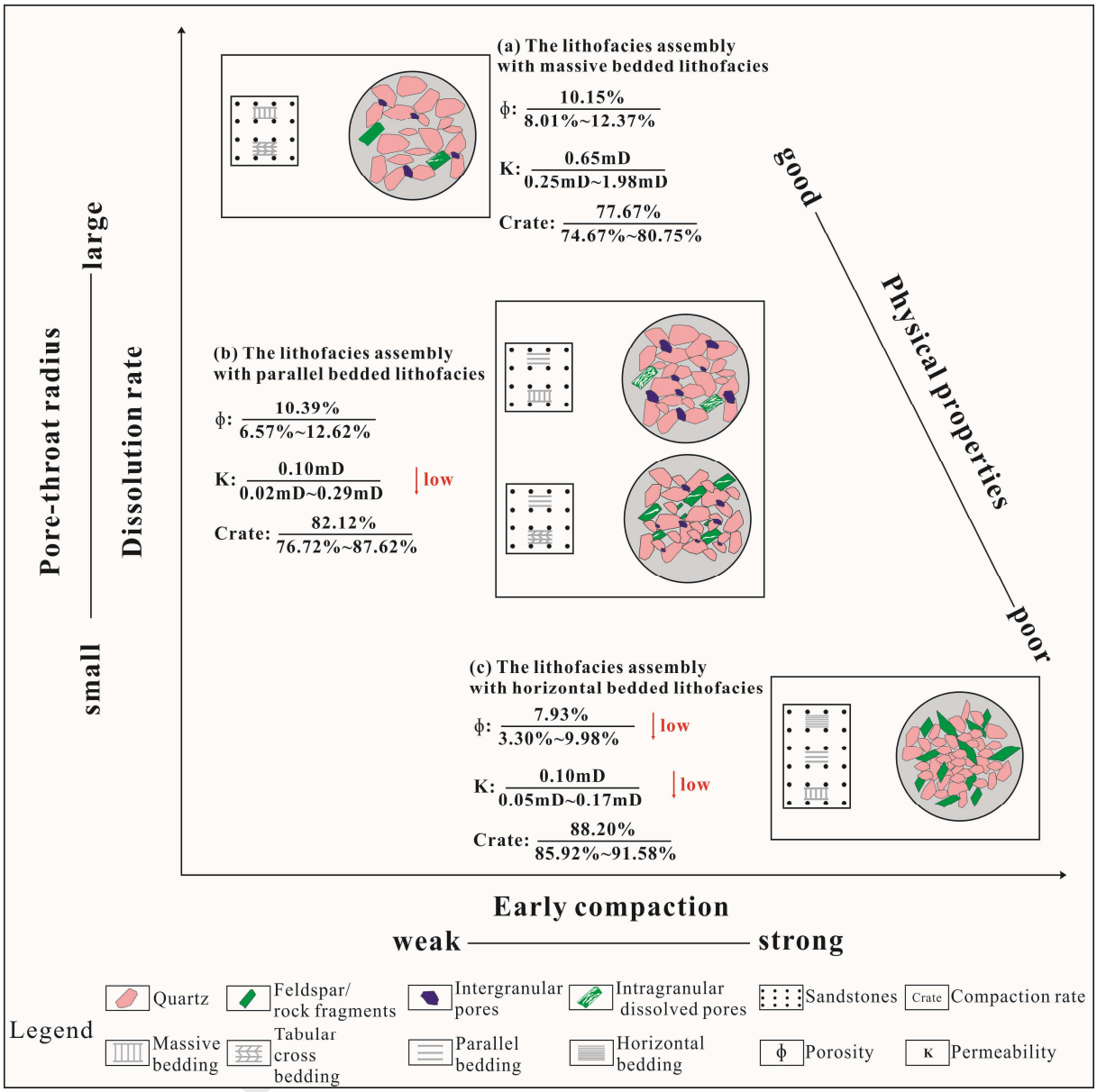

Figure 16 The schematic diagram shows the differential diagenesis controls on the physical properties of lithofacies in sandstone reservoirs

1. The physical properties of the assembly of massive bedded and tabular cross bedded lithofacies are better than that of the lithofacies assemblies containing parallel bedded lithofacies or horizontal bedded lithofacies.

2. The formation of lithofacies with different physical properties is controlled by the energy of sedimentary environment, mechanical differentiation, and differential diagenesis of lithofacies assemblies.

3. The direction of bedding can influence the degree of dissolution, and the development of parallel bedded lithofacies is beneficial for the dissolution rate of sandstones.

Declaration of interests

☒ The authors declare that they have no known competing financial interests or personal relationships that could have appeared to influence the work reported in this paper.

☐The authors declare the following financial interests/personal relationships which may be considered as potential competing interests: